

## MAGNETOHYDRODYNAMIC SIMULATIONS OF HOT JUPITER UPPER ATMOSPHERES

GEORGE B. TRAMMELL, ZHI-YUN LI &amp; PHIL ARRAS

Department of Astronomy, University of Virginia, P.O. Box 400325, Charlottesville, VA 22904-4325

## ABSTRACT

Two-dimensional simulations of hot Jupiter upper atmospheres including the planet's magnetic field are presented. The goal is to explore magnetic effects on the layer of the atmosphere that is ionized and heated by stellar EUV radiation, and the imprint of these effects on the Ly $\alpha$  transmission spectrum. The simulations are axisymmetric, isothermal, and include both rotation and azimuth-averaged stellar tides. Mass density is converted to atomic hydrogen density through the assumption of ionization equilibrium. The three-zone structure – polar dead zone, mid-latitude wind zone, and equatorial dead zone – found in previous analytic calculations is confirmed. For a magnetic field comparable to that of Jupiter, the equatorial dead zone, which is confined by the magnetic field and corotates with the planet, contributes at least half of the transit signal. For even stronger fields, the gas escaping in the mid-latitude wind zone is found to have a smaller contribution to the transit depth than the equatorial dead zone. Transmission spectra computed from the simulations are compared to HST STIS and ACS data for HD 209458b and HD 189733b, and the range of model parameters consistent with the data is found. The central result of this paper is that the transit depth increases strongly with magnetic field strength when the hydrogen ionization layer is magnetically dominated, for dipole magnetic field  $B_0 \gtrsim 10$  G. Hence transit depth is sensitive to magnetic field strength, in addition to standard quantities such as the ratio of thermal to gravitational binding energies. Another effect of the magnetic field is that the planet loses angular momentum orders of magnitude faster than in the non-magnetic case, because the magnetic field greatly increases the lever arm for wind braking of the planet's rotation. Spin-down timescales for magnetized models of HD 209458b that agree with the observed transit depth can be as short as  $\simeq 30$  Myr, much shorter than the age of the system.

*Subject headings:* (stars:) planetary systems - (magnetohydrodynamics:) MHD

## 1. INTRODUCTION

Hot Jupiters are gas giants orbiting close to their parent stars. The large stellar EUV flux heats and ionizes the upper atmosphere of these planets, increasing the thermal energy to a value approaching the gravitational binding energy, leading to a region weakly bound to the planet. The resulting large gas scale heights and atmospheric escape form an extended upper atmosphere around the planet, which may be probed by transmission spectroscopy using strong atomic resonance lines.

The existence of an extended upper atmosphere has been established through a variety of observations. Spectroscopic UV observations of HD 209458b (Henry et al. 2000) indicate a  $\sim 10\%$  decrease in flux during transit at  $\sim 100$  km s<sup>-1</sup> from the center of the hydrogen Ly $\alpha$  line. This transit depth has been attributed to an atmosphere of neutral H extending to a radius  $\simeq 2.4R_p$ , where  $R_p$  is the radius of the broadband photosphere of the planet (see Vidal-Madjar et al. 2008). As this radius is comparable to the Roche lobe radius, Vidal-Madjar et al. (2004) suggested that the planet is losing mass through Roche lobe overflow.

Additional observations of HD 209458b at transit have indicated absorption in other resonance lines, including NaI (Charbonneau et al. 2002; Sing et al. 2008), OI (Vidal-Madjar et al. 2004), CII (Vidal-Madjar et al. 2004; France et al. 2011), and SiIII (Linsky et al. 2010; France et al. 2011). Follow-up observations and re-analysis of HST-ACS data, in comparison with HST-STIS low and medium-resolution spectra, confirmed the

reduction of Ly $\alpha$  flux (Ehrenreich et al. 2008).

Transmission spectra of the hot Jupiter HD 189733b have also revealed absorption due to HI (in both Ly $\alpha$  and H $\alpha$ ; Lecavelier Des Etangs et al. 2010 and Jensen et al. 2012) and NaI (Redfield et al. 2008; Snellen et al. 2008). HST-COS observations by Linsky et al. (2010) have indicated absorption at up to  $\pm 50$  km s<sup>-1</sup> from line center in CII and SiIII that may be indicative of high velocity absorbers in the upper atmosphere (although these observations probe deeper layers than those probed by the HI observations). Multi-epoch spectra have also revealed significant changes in the Ly $\alpha$  transit depth, which are correlated with flares in ionizing radiation from the host star detected with HST and SWIFT (Lecavelier des Etangs et al. 2012).

This paper will focus on the Ly $\alpha$  absorption observed in the upper atmospheres of HD 209458b and HD 189733b. One interpretation of this absorption invokes hydrogen with thermal velocity  $\sim 10$  km s<sup>-1</sup> with such a large column density that the damping wings of Ly $\alpha$  become optically thick (e.g. Yelle 2004). Alternatively, a much smaller column is required if hydrogen atoms at thermal velocities  $\sim 100$  km s<sup>-1</sup>, created by charge exchange with stellar wind protons (Holmström et al. 2008; Ekenbäck et al. 2010; Tremblin & Chiang 2013), produce a sufficiently broad line profile.

This paper considers the former scenario in which the transit depth is due to a layer of thermal hydrogen in the planet's atmosphere. A number of studies have already explored the properties of strongly irradiated exoplanet atmospheres, and the possibility of thermally-driven hydrodynamic outflow (Yelle 2004, 2006; Tian et al.

2005; García Muñoz 2007; Murray-Clay et al. 2009; Ehrenreich & Désert 2011) and/or Roche Lobe overflow (Gu et al. 2003; Li et al. 2010; Lai et al. 2010; Ehrenreich & Désert 2011). The present study stands apart from the previous ones by including, through detailed magnetohydrodynamic (MHD) simulations, the effect of the planetary magnetic field. It is a follow-up of Trammell et al. (2011), which considered the magnetic effects semi-analytically.

Trammell et al. (2011, hereafter, Paper I) showed that the addition of the planetary magnetic field leads to the formation of an equatorial “dead-zone” (DZ) — a static region where the wind ram pressure is insufficient to overwhelm magnetic stresses and open the field lines into an outflow. This effect is well known in the classical MHD stellar wind theory (e.g. Mestel 1968). Paper I found a second static region near the poles where the wind can be shut off by the increased gravitational potential barrier from the stellar tide. In the strong tide limit, a wind-zone (i.e., the outflow region; WZ) is then expected to exist only at intermediate latitudes. A goal of the present paper is to verify this analytically-obtained three-zone structure with detailed numerical simulations.

Another conclusion from Paper I was that observations of Ly $\alpha$  absorption at the 5-10% level for HD 209458b may be detecting neutral H which is collisionally coupled to ionized gas confined to the equatorial DZ by the planet’s magnetic field. The bulk of the absorbing gas observed at transit thus may not be escaping, but rather is in the static equatorial dead zone. This qualitative result differs from the basic assumption in the hydrodynamic escape and Roche Lobe overflow models, that the transit observations are probing gas in the act of escaping from the planet.

A limitation of the analytic models in Paper I is that they ignore magnetic forces, which means that the poloidal magnetic geometry was assumed rather than computed self-consistently. Another limitation is that the fluid was assumed to corotate with the planet everywhere, including the wind zone, where the corotation is expected to break down at large distances. The treatment in this paper overcomes these limitations by performing MHD simulations, which compute the magnetic field structure and fluid rotation self-consistently. This allows a more accurate calculation of the mass and angular momentum loss rates, as well as the density and velocity profiles required to compute transmission spectra.

The plan of the paper is as follows. Section 2 describes the simulation setup and model parameters, and Section 3 presents the simulation results. Section 4 describes the method for computing model Ly $\alpha$  spectra. The frequency-dependent and frequency-integrated transit depths for a range of simulation parameters are compared with observations of HD 209458b and HD 189733b. Findings are summarized in Section 5. The Appendix contains a discussion of numerical effects at the shear layer separating the dead and wind zones.

## 2. SIMULATION SETUP

Consider a planet of mass  $M_p$  and radius  $R_p$  in a circular orbit at a distance  $D$  from a star of mass  $M_*$ . The planet’s rotation is synchronized to the orbit with angular velocity  $\Omega_p = [G(M_* + M_p)/D^3]^{1/2}$ , and the spin axis

is aligned with the orbital angular momentum. Outside the planet, in the region modeled by the simulations, the gas is not required to corotate with the planet.

Two-dimensional (2D), axisymmetric simulations in spherical coordinates are carried out with the publicly available MHD code ZEUS-MP (see Hayes et al. 2006, and references therein), which solves the ideal-MHD equations:

$$\frac{D\rho}{Dt} = -\rho\nabla \cdot \mathbf{v} \quad (1)$$

$$\rho \frac{D\mathbf{v}}{Dt} = -\nabla P + \frac{1}{4\pi}(\nabla \times \mathbf{B}) \times \mathbf{B} - \rho\nabla U \quad (2)$$

$$\frac{\partial \mathbf{B}}{\partial t} = \nabla \times (\mathbf{v} \times \mathbf{B}), \quad (3)$$

where the comoving (Lagrangian) derivative is defined as

$$\frac{D}{Dt} \equiv \frac{\partial}{\partial t} + \mathbf{v} \cdot \nabla. \quad (4)$$

Equations 1-3 are the mass continuity, momentum and induction equation, respectively. The neglect of explicit fluid viscosity in Equation 2 and resistivity in Equation 3 are discussed in Appendix B of Paper I. The quantity  $U$  is an effective potential to be defined below, and other symbols have their standard meaning.

Instead of solving the energy equation, an isothermal equation of state,  $P = \rho a^2$ , is used, where  $a$  is the (constant) isothermal sound speed. This assumption is equivalent to adding energy to the flow to counter adiabatic cooling. It gives rise to a transonic outflow (e.g. Lamers & Cassinelli 1999). The isothermal assumption is convenient for the present study, where the focus is not on the initial launching of the wind, but rather on magnetic effects. A more detailed study, beyond the scope of this paper, would include heating and cooling effects in an energy equation. Note, however, that since the magnetic field and rotation are included, the flow is also accelerated in part by the “magneto-centrifugal” effect (Blandford & Payne 1982), as well as stellar tides.

The computational grid extends from an inner radial boundary at  $r = R_p$  to the outer boundary at  $r = 30R_p$ , with  $R_p$  set to the planet’s observed transit continuum radius (Southworth 2010), and from the north pole at  $\theta = 0$  to the south pole at  $\theta = \pi$ . The radial box size was chosen through experimentation so that all MHD critical points in the wind zone were contained within the computational domain for a wide range of model parameters. The standard resolution is  $272 \times 200$ , with the radial cell size  $\Delta r = r_{i+1} - r_i$  increasing outward according to  $\Delta r_{i+1}/\Delta r_i = 1.02$ ; the ratio was chosen to adequately resolve the wind acceleration region near the base. The  $\theta$  grid is uniformly spaced. Surrounding the active grid are two layers of ghost zones at each of the four boundaries; they are used to impose boundary conditions.

At time  $t = 0$ , the fluid is uniformly rotating with velocity  $(v_r, v_\theta, v_\phi) = (0, 0, \Omega_p r \sin \theta)$ , and in hydrostatic balance over most of the computational grid. The initial magnetic field is assumed to be a potential field, so that the magnetic force is everywhere zero, an assumption consistent with the equation of hydrostatic balance. In a reference frame corotating with the planet, and with

the origin comoving with the planet, hydrostatic balance takes the form (Paper I)

$$0 = -a^2 \nabla \rho - \rho \nabla U_{\text{rot}}. \quad (5)$$

The potential  $U_{\text{rot}}$  includes contributions from the gravity of the planet, the stellar gravity, the dipole term arising from the acceleration of the origin, and the centrifugal force, and takes the form

$$U_{\text{rot}}(\mathbf{x}) = -\frac{GM_p}{|\mathbf{x}|} - \frac{GM_\star}{|\mathbf{x} - \mathbf{x}_\star|} + \frac{GM_\star \mathbf{x} \cdot \mathbf{x}_\star}{|\mathbf{x}_\star|^3} - \frac{1}{2} |\boldsymbol{\Omega}_p \times \mathbf{x}|^2 \quad (6)$$

The dipole term, which acts to accelerate the center of mass of the planet, cancels off part of the stellar gravity, leaving only a tidal acceleration. Expressing the position vector in spherical coordinates  $\mathbf{x} = (r, \theta, \phi)$ , the position of the star as  $\mathbf{x}_\star = (D, \pi/2, 0) = D\mathbf{e}_x$ , and making the tidal approximation,  $r \ll D$ , gives

$$U_{\text{rot}}(\mathbf{x}) \simeq -\frac{GM_p}{r} - \frac{1}{2} \Omega_p^2 r^2 (f_{\text{rot}} \sin^2 \theta - 1), \quad (7)$$

where the longitude-dependent function  $f_{\text{rot}} = 1 + 3 \cos^2 \phi$ . As the simulations are axisymmetric, we substitute the azimuthal average  $\cos^2 \phi \rightarrow 1/2$ , yielding  $f_{\text{rot}} = 5/2$ . At the equator, the radial acceleration  $\partial U_{\text{rot}}/\partial r = 0$  at the radius

$$r_{\text{H}} = \left( \frac{2GM_p}{3\Omega_p^2} \right)^{1/3} \simeq D \left( \frac{2M_p}{3M_\star} \right)^{1/3}, \quad (8)$$

a factor of  $2^{1/3}$  larger than the physically correct value for the Lagrange points, which are evaluated along the star-planet line. In this paper  $r_{\text{H}}$  will be called the Hill radius.

Substituting Equation 7 into Equation 5, the initial density distribution over the inner part of the computational domain takes the form

$$\rho(r, \theta) = \rho_{\text{ss}} \exp \left[ - \left( \frac{U_{\text{rot}}(r, \theta) - U_{\text{rot}}(R_p, \pi/2)}{a^2} \right) \right], \quad (9)$$

where  $\rho_{\text{ss}}$  is the density at  $(r, \theta) = (R_p, \pi/2)$ . The initial density distribution then requires  $a$  and  $\rho_{\text{ss}}$  as parameters, in addition to the parameters of the planet, star and orbit. Well outside  $r_{\text{H}}$ , the hydrostatic density profile rises steeply to large values, due to the net acceleration pointing outward. For the initial condition only, a ceiling is placed on the density at  $\rho \leq \rho_{\text{ss}}$  to limit this growth. In the outer regions of the computational grid where  $\rho = \rho_{\text{ss}}$ , the pressure force is then zero and the tidal and centrifugal forces pull mass outward, initiating the outflow. Since the physical, steady-state solutions exhibit  $\rho \ll \rho_{\text{ss}}$  in the outer regions, capping the density is a device to allow the density to decrease to physical levels more quickly.

It is simpler to perform the simulation not in a corotating frame, which would require the addition of Coriolis and centrifugal forces, but rather in a non-rotating frame. The origin still moves with the center of the planet. In this reference frame, the centrifugal term can be omitted

from the potential, giving

$$U(\mathbf{x}) = -\frac{GM_p}{|\mathbf{x}|} - \frac{GM_\star}{|\mathbf{x} - \mathbf{x}_\star|} + \frac{GM_\star \mathbf{x} \cdot \mathbf{x}_\star}{|\mathbf{x}_\star|^3} \simeq -\frac{GM_p}{r} - \frac{1}{2} \Omega_p^2 r^2 (f \sin^2 \theta - 1), \quad (10)$$

where now  $f = 1 + \cos^2 \phi$ . The azimuthal average gives  $f = 3/2$  for the non-rotating frame. The  $r$  and  $\theta$  components of  $-\nabla U$  from Equation 10 are introduced into the Zeus-MP code as a source term in the momentum equations. Since the gas is not required to corotate, Equation 8 may underestimate the radius at which the equatorial acceleration changes sign. An upper limit is found by ignoring the centrifugal force. Using  $f = 3/2$  with Equation 10 would give  $(2GM_p/\Omega_p^2)^{1/3}$  for this radius, larger than the expression in Equation 8 by a factor  $3^{1/3}$ .

The initial condition for the magnetic field is a dipole with magnetic axis aligned with the rotation axis:

$$B_r = B_0 \left( \frac{r}{R_p} \right)^{-3} \cos \theta \quad (11)$$

$$B_\theta = \frac{B_0}{2} \left( \frac{r}{R_p} \right)^{-3} \sin \theta \quad (12)$$

$$B_\phi = 0, \quad (13)$$

where the field at the magnetic pole is  $B_0$ . The development of nonzero  $B_\phi$  at  $t > 0$  will lead to magnetic torques on the gas and planet. A key parameter of the model is the equatorial value of the plasma  $\beta$  at the inner radius:

$$\beta_0 = \frac{8\pi P_{\text{ss}}}{(B_0/2)^2} \quad (14)$$

where  $P_{\text{ss}} = a^2 \rho_{\text{ss}}$  is the base pressure at the equator, and  $B_0/2$  is the magnetic field at the equator. This parameter sets the size of the equatorial DZ (Paper I).

Compared with the initial conditions, the boundary conditions are much more difficult to implement, especially on the inner radial boundary, which is the base of both the wind and dead zones. Since the boundary conditions are crucial to the success of the numerical simulations, they will be described in some detail.

Consider first the boundary condition on  $\rho$  at the inner radial boundary. The densities in the inner radial ghost zones and the first radial active zones are kept at their initial values at all times. Even though the densities in the first active zones are updated at each time step, the updated values are discarded and replaced by their initial values. This guarantees that the base density is held fixed at the prescribed value, even in the wind zone.

For the inner radial boundary,  $v_r = 0$  is set at the inner face of the first active zone, as well as in the ghost zones. In other words,  $v_r(R_p, \theta) = 0$  and  $v_r(r^-, \theta) = 0$ , where  $r^- (< R_p)$  denotes the inner radial ghost region. The reflection boundary condition is applied to  $v_\theta$ , so that  $v_\theta(r^-, \theta) = v_\theta(r^+, \theta)$ , where  $r^+$  is the symmetry point (with respect to the  $r = R_p$  surface) in the active domain of the location  $r^-$  in the ghost region. The boundary condition on the azimuthal velocity component,  $v_\phi$ , is  $v_\phi(r^-, \theta) = 2v_\phi(R_p, \theta) - v_\phi(r^+, \theta)$  where  $v_\phi(R_p, \theta) = \Omega_p R_p \sin \theta$ . That is, the average of the first

ghost zone and the first active zone should equal the corotation velocity. It has been verified that, in the absence of magnetic field, rotation and stellar tides, the inner hydro boundary conditions produce a thermally driven wind that matches, in steady state, the well-known analytical solution.

The magnetic boundary conditions at the inner radial boundary are more complicated to implement. They are enforced through the electromotive force (EMF)  $\epsilon = \mathbf{v} \times \mathbf{B}$ , as this will automatically preserve  $\partial(\nabla \cdot \mathbf{B})/\partial t = 0$  during the time evolution. In 2D (axisymmetric) geometry, only the  $r$ - and  $\theta$ -components of  $\epsilon$  affect  $B_\phi$ :

$$\frac{\partial B_\phi}{\partial t} = \frac{1}{r} \left[ \frac{\partial}{\partial r}(r\epsilon_\theta) - \frac{\partial \epsilon_r}{\partial \theta} \right]. \quad (15)$$

Although  $B_\phi$  is assumed to be zero initially in our simulation, it can grow with time, particularly in the outflow region. The boundary conditions on  $\epsilon_r$  and  $\epsilon_\theta$  are designed to enable  $B_\phi$  in the ghost zones to grow at the same rate as in the active zones. Specifically, we demand

$$\frac{\epsilon_r(r^-)}{r^-} = \frac{\epsilon_r(r^+)}{r^+}, \quad (16)$$

and

$$\left[ \frac{1}{r} \frac{\partial}{\partial r}(r\epsilon_\theta) \right]_{r^-} = \left[ \frac{1}{r} \frac{\partial}{\partial r}(r\epsilon_\theta) \right]_{r^+}. \quad (17)$$

The value of  $\epsilon_\theta$  in the ghost zone is determined by equation 17 together with the condition

$$\epsilon_\theta(R_p, \theta) = \Omega_p R_p \sin \theta B_r(R_p, \theta), \quad (18)$$

which ensures that the footpoints of the magnetic field lines corotate with the planet.

For  $\epsilon_\phi = v_r B_\theta - v_\theta B_r$ , the boundary condition  $\epsilon_\phi(R_p, \theta) = 0$  enforces poloidal velocity parallel to poloidal magnetic field at  $r = R_p$ . The use of this “flux freezing” condition for the magnetic field is justified in Appendix B of Paper I. It also guarantees that  $B_r(r = R_p)$  remains unchanged, i.e., the footpoints of the field lines are firmly anchored on the rotating inner radial boundary. For  $\epsilon_\phi$  in the ghost zone,  $\epsilon_\phi(r^-) = -\epsilon_\phi(r^+)$  is enforced so that the radial gradient of  $\epsilon_\phi$ , which controls the evolution of  $B_\theta$ , is continuous across the inner radial boundary. This set of magnetic boundary conditions is similar to that used successfully by Krasnopolsky et al. (1999, 2003) to simulate disk-driven magnetocentrifugal winds.

The standard “outflow” boundary condition implemented in ZeusMP is used at the outer radial boundary, with all hydrodynamic variables and the three components of the EMF projected to zero slope. In addition,  $\partial B_\phi/\partial t = 0$  is set for the outer radial ghost zones, which was found to prevent the growth of unphysically large currents that sometimes develop near the outer boundary. At the  $\theta = 0$  and  $\theta = \pi$  boundaries, the standard “axial” boundary condition as implemented in ZeusMP is used, which enforces reflection symmetry for the  $r$ -component of the velocity and magnetic field; the  $\theta$ - and  $\phi$ -components are reflected with a change of sign.

The simulations were evolved until a steady-state solution was achieved. A summary of the main model parameters is shown in Tables 1 and 2.

TABLE 1  
PRIMARY MODEL PARAMETERS

Parameter	Range	Description
$R_p$	$1.35 R_{Jup}$	planet radius
$\rho_{ss}$	$\sim 10^{-16} - 10^{-13} \text{ g cm}^{-3}$	substellar point mass density
$a$	$9\text{-}11 \text{ km s}^{-1}$	isothermal sound speed
$B_0$	$1.0\text{-}100 \text{ G}$	polar magnetic field strength
$M_p$	$0.7 M_{Jup}$	planet mass
$M_\star$	$1.1 M_\odot$	host stellar mass
$D$	$0.035\text{-}0.06 \text{ AU}$	orbital separation

NOTE. — Description and range of the model parameters used in the simulations.

TABLE 2  
PARAMETERS FOR HD 209458B RUNS

Run	$D$ (AU)	$P_{ss}$ ( $\mu\text{bar}$ )	$a$ (km/s)	$B_0$ (G)	$\beta_0$
Model 1	0.047	0.05	10.0	10.0	0.051
Model 2	0.047	0.05	10.0	1.0	5.1
Model 3	0.047	0.05	10.0	50.0	0.002
Model 4	0.047	0.05	9.0	10.0	0.041
Model 5	0.047	0.05	11.0	10.0	0.061
Model 6	0.047	0.005	10.0	10.0	0.0051
Model 7	0.047	0.5	10.0	10.0	0.51
Model 8	0.035	0.05	10.0	10.0	0.051
Model 9	0.06	0.05	10.0	10.0	0.051
Model 10	0.047	0.05	10.0	100.0	0.0005

NOTE. — This table contains simulation parameters varying a single parameter ( $B_0$ ,  $D$ ,  $a$ ,  $P_{ss}$ ) relative to the fiducial case (Model 1). The planetary radius and mass are fixed to  $R_p = 1.35 R_J$ ,  $M_p = 0.7 M_J$ . The values of  $\beta_0$  can be compared to the value  $\beta_{0,Jup} = 0.069$  using Jupiter’s magnetic field and a base pressure  $P_{ss} = 0.05 \mu\text{bar}$ .

### 3. SIMULATION RESULTS

A fiducial model is chosen with HD 209458b’s parameters and  $B_0 = 10 \text{ G}$  (Model 1 in Table 2). The other simulations listed in Table 2 vary the model parameters listed in Table 1. A qualitative discussion of the simulation results is given in § 3.1, and a more quantitative analysis in § 3.2. The last subsection (§ 3.3) contains a discussion of mass and angular momentum loss rates from the planet.

#### 3.1. Qualitative Results: Magnetic Field and Tidal Strength

One of the most important qualitative results of this paper is the confirmation of the three-zone structure of the magnetosphere predicted analytically in Paper I. The three distinct regions are clearly visible in Figures 1 and 2 — (1) an equatorial dead-zone (DZ) containing static gas confined by the magnetic field, (2) a wind-zone (WZ) where an outflow is driven along open magnetic field lines, and (3) a second polar DZ where the stellar tide has shut off the outflow (see also Fig. 7 of Paper I). The range of magnetic field and stellar tide over which the equatorial and polar DZ’s exist has been discussed in Paper I. Roughly, the equatorial DZ requires  $\beta_0 \lesssim 1$ , i.e. the magnetic pressure dominates gas pressure at the base of the atmosphere (the hydrogen ionization zone) at the equator. The existence of the polar dead zone, and the inability to drive a transonic outflow there, occurs inside a critical orbital separation. Roughly, this criterion

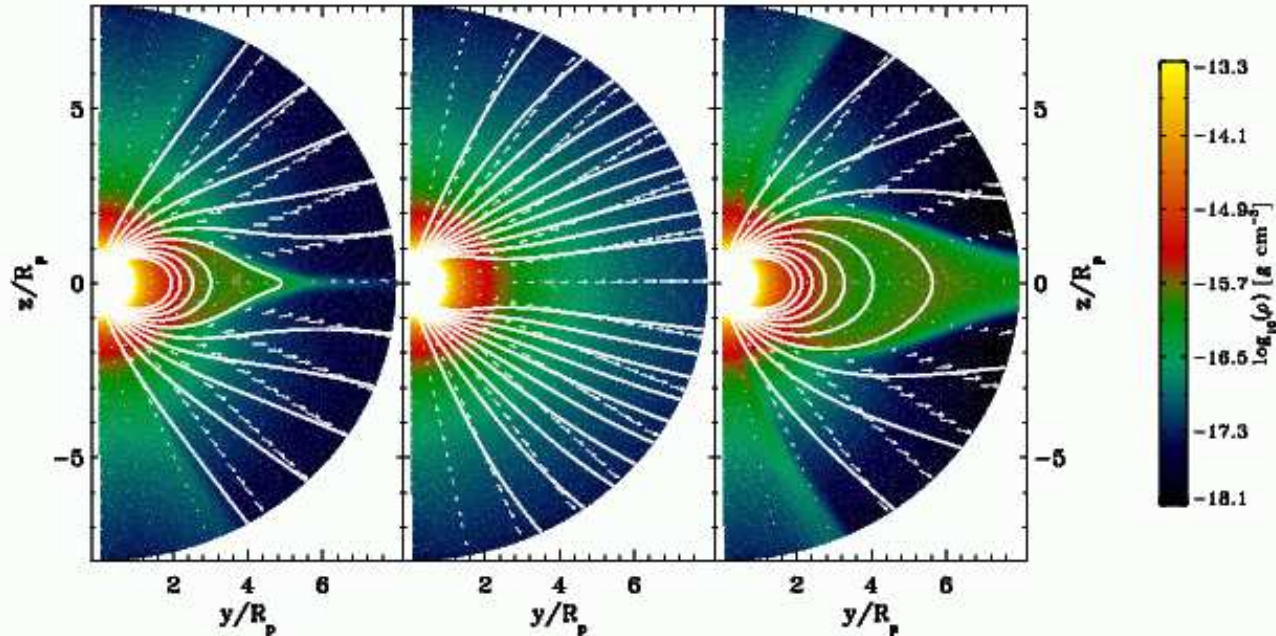


FIG. 1.— Contours of total gas density  $\rho(r, \theta)$  in units of  $\text{g cm}^{-3}$  as viewed during transit, illustrating the effect of the magnetic field (white lines) on the size of the equatorial DZ. *Left*: Model 1 (fiducial model with  $B_0 = 10$  G) *Center*: Model 2 ( $B_0 = 1$  G) *Right*: Model 3 ( $B_0 = 50$  G). For these three models, the remaining parameters given in Table 2 are otherwise identical. White arrows indicate the direction and magnitude of the poloidal fluid velocity. Only the inner  $8 R_p$  portion of the grid is shown (the magnetic field lines near the planet are not drawn for clarity).

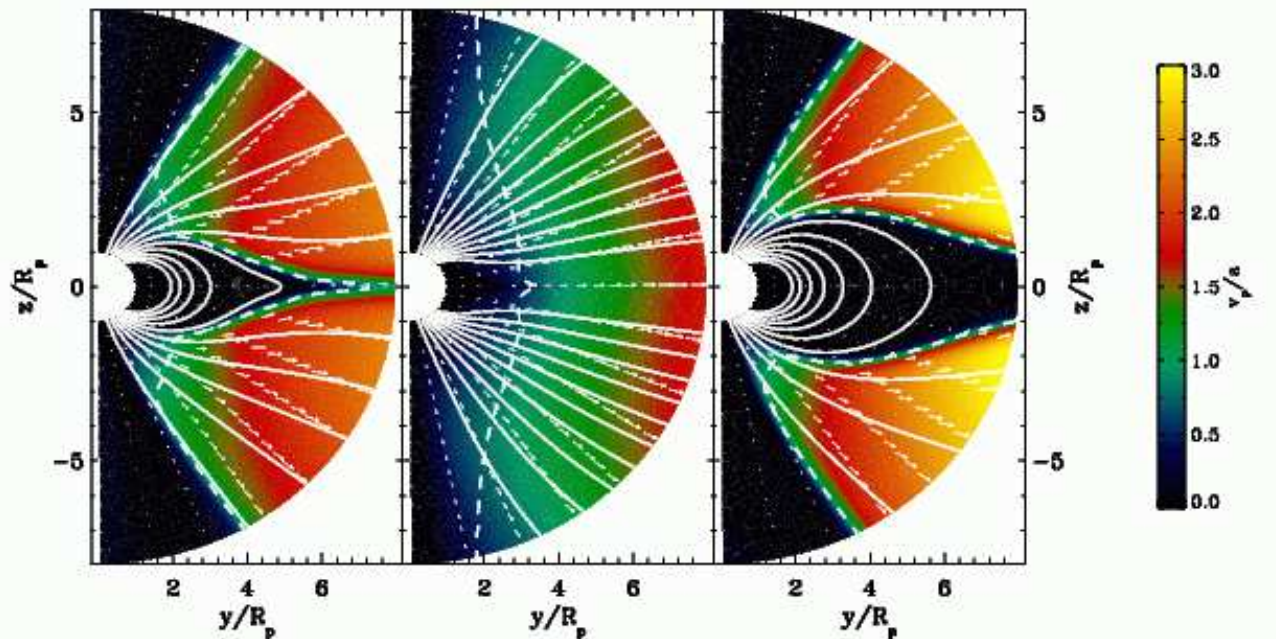


FIG. 2.— Similar to Figure 1, but for contours of poloidal velocity  $v_p$  in units of the isothermal sound speed  $a$ . *Left*: Model 1 (fiducial model) *Center*: Model 2 *Right*: Model 3 for parameters given in Table 2. White-dashed contours trace the (slow magneto-)sonic points, which trace the vicinity of the shear layers separating the static DZs (i.e., darkest contours) from the transonic WZs.

translates into the rotation velocity  $\Omega_p$  at the fiducial sonic point radius  $r_{s,0} = GM_p/3a^2$  must be supersonic,  $\Omega_p r_{s,0} \gtrsim a$  (cf. Equation 36 of Paper I).

The DZ-WZ boundaries in the simulation contain a shear layer separating the outflowing gas in the WZ from the static gas in the DZ. In addition, the magnetic field changes rapidly in this boundary layer, implying a current sheet. The origin of this current sheet is that, for identical Bernoulli constant at the inner boundary, the

WZ has smaller density compared to the neighboring DZ by a factor  $\sim \exp(-v_p^2/a^2)$  (Mestel and Spruit 1987; Paper I), where  $v_p$  is the poloidal wind speed. Since the total pressure, gas plus magnetic, must be continuous across the boundary, the decrease in gas pressure implies an increase in magnetic pressure, and hence a current sheet. Numerical issues related to the shear in velocity and magnetic field will be discussed further in the Appendix.

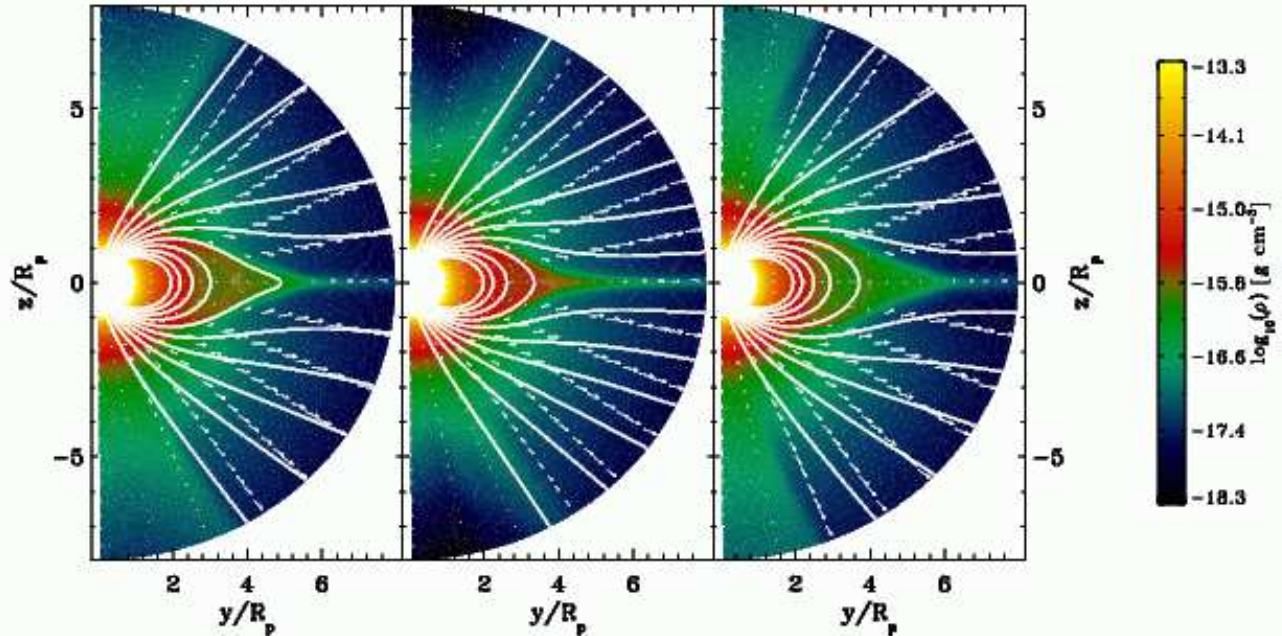


FIG. 3.— Similar to Figure 1, illustrating how the stellar tide influences the size of the equatorial/polar DZs. All panels have the same parameters as Model 1 of Table 2, except for the varying orbital distance  $D$ . *Left*: the fiducial Model 1 for HD 209458b with  $D = 0.047$  AU. *Center*: Model 8 ( $D = 0.035$  AU), which illustrates the effect of increasing the stellar tide by shrinking the planet’s orbit. *Right*: Model 9 ( $D = 0.06$  AU). Note that the polar DZ size is larger and equatorial DZ smaller for the stronger tide case (middle panel), as can be seen by the range of angles with zero-length velocity vectors (white arrows). As in Figure 1, the innermost magnetic field lines have been suppressed for clarity.

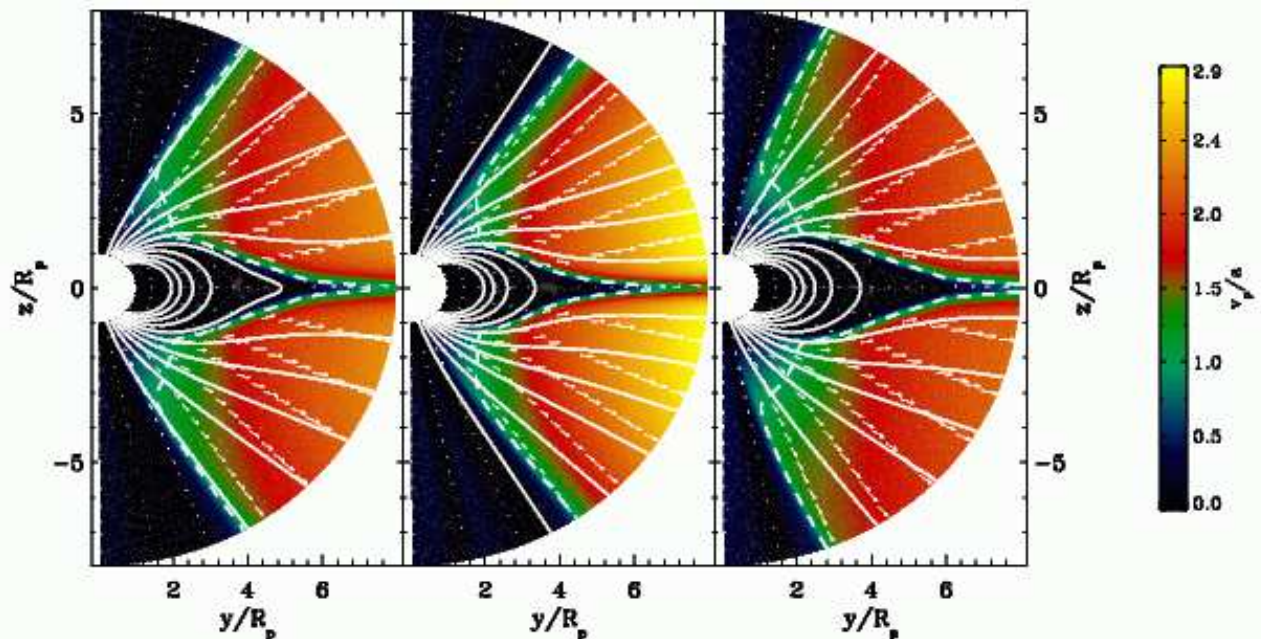


FIG. 4.— Similar to Figure 3, showing the 2D structure of the poloidal velocity  $v_p$  field, in units of the isothermal speed  $a$  for the same three models shown in Figure 3. Higher stellar tide pushes the slow magnetosonic point inward at mid-latitudes and leads to a stronger outflow ram pressure, which can open a larger region of the planetary magnetic field lines and decrease the size of the equatorial DZ.

Figure 1 illustrates the effect of the magnetic field on the density profile in the magnetosphere. The parameters for the runs in each panel are identical except for the magnetic field, with  $B_0 = 10, 1$  and  $50$  G from left to right, respectively (Models 1-3 in Table 2). As predicted in Paper I and expected intuitively, the size of the equatorial DZ increases with the field strength, when all other parameters are held fixed. For a dipole

field line with a footpoint at  $\theta_0$ , the magnetic pressure at the looptop at the equator decreases outward as  $B^2 \propto (1 - 3 \sin^2 \theta / 4) \sin^{12} \theta_0 / \sin^{12} \theta$ , and so field lines nearer the pole, with smaller  $\theta_0$ , suffer a larger decrease in magnetic pressure from pole to equator. The larger DZ size for larger  $B_0$  then reflects the inability of ram pressure to overcome magnetic pressure, except in a smaller region near the pole where the field decreases outward

more rapidly.

The observational implication of the increase of DZ size with magnetic field is that more of the circum-planetary material is expected to be confined within the static dead zone, which should make this region easier to probe with transit observations (see Section 4). A weaker magnetic field  $B_0 \ll 1$  G would not significantly confine the gas, and a larger range of latitudes will participate in the outflow.

To more clearly differentiate the polar/equatorial DZs from the neighboring WZ, we plot in Figure 2 the poloidal velocity for the same Models 1-3 shown in Figure 1. The more dramatic contrast between the static DZ regions, where the fluid velocity is very subsonic, and the WZ with transonic outflow further illustrates the existence of the polar/equatorial DZs. The changing colors show the accelerating outflow in the mid-latitude regions along open magnetic field lines that have been combed out by currents in the magnetosphere. The darkest regions can be compared to the highest density regions in Figure 1.

Besides the field strength  $B_0$ , the structure of the magnetosphere is also influenced by the stellar tide. The tidal effects are illustrated in Figures 3 and 4. All parameters except  $D$  are held fixed, even though temperature would likely increase as the planet is moved nearer the star. The left panel is the fiducial Model 1. In the middle panel (Model 8), the orbital distance has been decreased to  $D = 0.035$  AU, so that the stellar tide is stronger than that for HD 209458b ( $D = 0.047$  AU). As predicted in Paper I, the stronger stellar tide increases the outward acceleration of the mid-latitude outflow by moving the sonic point inward. It results in an equatorial DZ that is slightly smaller in size but denser at the same distance from the planet relative to Model 1. Figure 4 shows that the polar DZ size is also larger for the stronger tide case, as can be seen by the range of angles occupied by largely subsonic gas with small poloidal velocities, again in broad agreement with the analytic results of Paper I.

### 3.2. Quantitative Analysis: Density and Velocity Profiles

To examine the numerical simulations in more detail, Figure 5 shows the run of density and poloidal velocity along three different co-latitudes for the fiducial Model 1. The  $\theta$  values are chosen to highlight the separate polar DZ, WZ and equatorial DZ regions, respectively.

Along  $\theta \approx 0$ , near the pole, the density decreases rapidly with  $r$  because the downward gravity of the planet and star must be balanced by pressure gradient in hydrostatic equilibrium. For this region, the flow speed remains well below the sound speed, in agreement with Paper I, which predicts the absence of a transonic solution in the polar region. The  $\theta \approx \pi/4$  line initially passes through the equatorial dead zone (where the poloidal velocity is close to zero; see the second panel of Figure 5), before entering the wind zone. In the wind zone, the flow speed increases away from the planet, reaching nearly twice the sound speed at  $r = 8R_p$ . The density drops with distance accordingly.

The density distribution along the equator at  $\theta \approx \pi/2$  is the most intriguing. After an initial rapid decrease, it increases for a short distance near  $r \approx 3R_p$ , and then resumes a slow decline. Such a ‘‘bump’’ in the density

profile was predicted in Paper I, for the gas outside the Hill radius, yet still confined inside the static magnetosphere. This is a consequence of the outward pointing gravity outside the Hill radius in Equation 8, causing the density to increase outward instead of inward. However, the outward increase in figure 5 occurs well inside  $r_H \approx 5.4R_p$ ! Hence it cannot be due to the change in the sign of gravity. In the Appendix the origin of this density increase is explored, and seems to be due to viscous stresses associated with numerical effects near the equatorial DZ/WZ boundary. As the numerical resolution is increased, the density bump in figure 5 decreases in size. In the Appendix it is shown that increasing the resolution has a  $\lesssim 1\%$  effect on the integrated transit depth, even as the density bump decreases. This gives confidence that resolution-dependent effects are not leading to large errors in the transit depth.

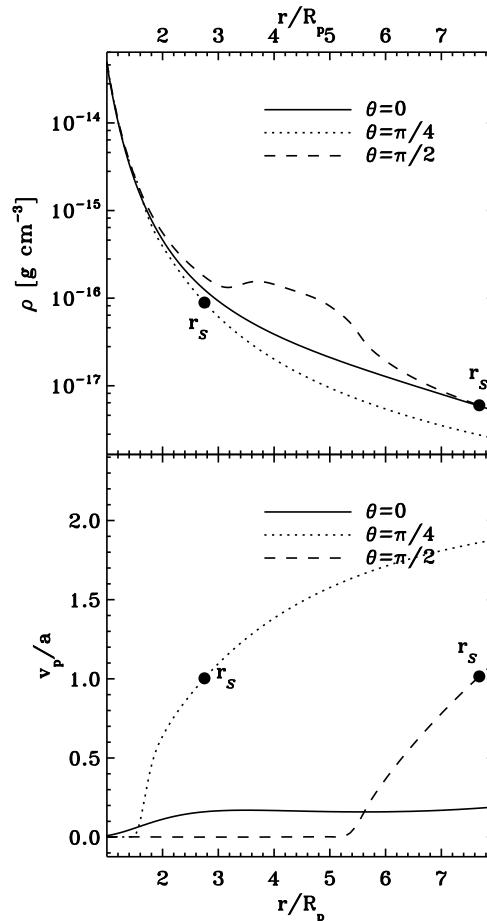


FIG. 5.— 1D radial profiles of density  $\rho(r)$  (top) and poloidal velocity  $v_p(r)$  (bottom) in units of the sound speed  $a$  for the fiducial Model 1 at three representative angles. The three angles shown in each panel are  $\theta \approx 0$  (solid black line),  $\theta \approx \pi/4$  (dotted black line), and  $\theta \approx \pi/2$  (dashed black line). Sonic point locations are indicated by the black symbols labeled  $r_s$ .

### 3.3. Mass and Angular Momentum Loss Rates

The MHD simulations presented in this paper allow a more accurate determination of the rates of mass and angular momentum losses ( $\dot{M}$  and  $\dot{J}$ ) as compared

to the semi-analytic solutions from Paper I, since here the magnetic field geometry and fluid velocity are self-consistently computed. These quantities are computed as a function of  $r$  by integrals over  $\theta$ :

$$\dot{M}(r) = 2\pi r^2 \int_0^\pi d\theta \sin\theta \rho(r, \theta) v_r(r, \theta) \quad (19)$$

and

$$\dot{J}(r) = 2\pi r^3 \int_0^\pi d\theta \sin^2\theta \times \left[ \rho(r, \theta) v_r(r, \theta) v_\phi(r, \theta) - \frac{B_r(r, \theta) B_\phi(r, \theta)}{4\pi} \right] \quad (20)$$

Typically  $\dot{M}(r)$  and  $\dot{J}(r)$  are constant with radius to better than 1%, which provides a check on the accuracy of the numerical solutions. Table 3 summarizes the results for  $\dot{M}$  and  $\dot{J}$  for Models 1-10.

The planet's magnetic field affects the dynamics in several ways. A stronger magnetic field increases the size of the equatorial DZ, restricting the WZ to a smaller range of latitudes. Therefore, one might expect that the mass-loss rate will decrease for a stronger magnetic field. This expectation is born out in the  $\dot{M}$  values presented in Table 3, where the mass loss decreases by  $\sim 35\%$  for a factor of 5 increase in  $B_0$  from Model 1 to Model 3. Despite the reduction in  $\dot{M}$ , the total angular momentum loss rate  $\dot{J}$  increased by a factor of  $\sim 2.5$ , implying an increase in loss of specific angular momentum,  $\dot{J}/\dot{M}$ , due to a longer magnetic lever arm for the torque. The effect of the magnetic field and tides on the specific angular momentum loss is most clearly displayed in column 4 of Table 3. The quantity  $\dot{J}/(\dot{M}\Omega_p R_p^2)$  has the value 2/3 ignoring these effects (Mestel 1968), but is significantly larger here, even for relatively weak field cases. Conversely, for a weaker magnetic field (i.e., Model 2),  $\dot{M}$  is larger due to the larger range of latitudes in the WZ (see the center panel of Figure 2).

Stronger tides result in a slightly smaller equatorial DZ, because the outward tidal force can open more magnetic field lines, but a larger polar DZ, due to the increased potential barrier. Stronger tide also moves the sonic point inward, which tends to increase  $\dot{M}$ . For example,  $\dot{M}$  of the stronger tide Model 8 is increased slightly, by a factor of  $\simeq 20\%$ , compared to Model 1. Presumably if the tide is increased to the point that the sonic point moves all the way in to the steeply-rising density profile deeper in the atmosphere, this (figure 5) will result in a greater sensitivity to the strength of the tide, as is expected for Roche lobe overflow.

A much larger change in  $\dot{M}$  comes from varying the base pressure  $P_{ss}$  (Models 6 and 7) or the isothermal sound speed  $a$  (Models 4 and 5). For example, when  $P_{ss}$  increases by a factor of 10, from 0.05 to 0.5  $\mu\text{bar}$ ,  $\dot{M}$  rises by a factor of 16.9. When  $a$  increases by 10%, from 10 to 11 km/s,  $\dot{M}$  shoots up by a factor of 4.16! In the more heavily mass-loaded winds, the field lines bend backward significantly in the azimuthal direction relatively close to the planet, forcing the fluid to rotate substantially below the corotation speed. The self-consistent treatment of the deviation from corotation here is an improvement over the analytic solutions of Paper I. Con-

TABLE 3  
MASS/ANG. MOM. LOSS RATES (HD 209458B)

Run	$\dot{M}$	$\dot{J}$	$\dot{J}/(\dot{M}\Omega_p R_p^2)$	$\delta F/F$
Model 1	3.29	10.20	162.24	0.100
Model 2	6.12	1.17	9.97	0.125
Model 3	2.11	26.40	655.64	0.157
Model 4	0.48	3.74	404.68	0.048
Model 5	13.70	19.05	72.81	0.209
Model 6	0.25	2.20	455.36	0.028
Model 7	55.50	37.59	35.46	0.470
Model 8	3.89	15.24	131.92	0.154
Model 9	3.21	7.04	165.70	0.088
Model 10	2.87	33.40	610.59	0.253

NOTE. — Mass-loss rates  $\dot{M}$  [ $10^{11}$  g s $^{-1}$ ] and angular momentum loss rates  $\dot{J}$  [ $10^{28}$  g cm $^2$  s $^{-2}$ ] for the 9 models with parameters specified in Table 2, along with the corresponding integrated Ly $\alpha$  transit depth  $\delta F/F$  (see Equation 26) from -200 to +200 km s $^{-1}$  from line center.

versely, a smaller  $P_{ss}$  or  $a$  leads to a lower  $\dot{M}$ , and a wind that is dominated by the magnetic field out to a larger distance. It is interesting to note that the ratio  $\dot{J}/(\dot{M}\Omega_p R_p^2)$  has rather large values of 404.68 and 455.36 for Model 4 ( $a = 9$  km/s) and 6 ( $P_{ss} = 0.005$   $\mu\text{bar}$ ), respectively. They are very different from the purely hydro winds from the planet, where the ratio is 2/3. The relatively low mass loss rate in these cases allows the magnetic field to effectively enforce corotation up to a distance of  $\sim 20 R_p$ .

The large spin-down torques found in the strongly magnetized models may torque the planet away from synchronous rotation (Paper I). Defining  $\Gamma = \dot{J}/(\dot{M}\Omega_p R_p^2)$  and  $J = \alpha M R_p^2 \Omega_p$ , the spindown timescale is

$$\frac{J}{\dot{J}} = \frac{\alpha}{\Gamma} \left( \frac{M}{\dot{M}} \right) \simeq 3 \times 10^7 \text{ yr} \left( \frac{\alpha}{0.1} \right) \left( \frac{660}{\Gamma} \right) \left( \frac{M}{0.7 M_J} \right) \left( \frac{2 \times 10^{11} \text{ g s}^{-1}}{\dot{M}} \right) \quad (21)$$

for Model 3 parameters. In torque equilibrium between magnetic spin-down torques and gravitational tidal torques, a steady-state asynchronous spin rate would occur, with associated steady-state gravitational tide heating. However, deviations from synchronous rotation depend on strength of the planet's tidal dissipation, which is uncertain, but likely to give synchronization timescales orders of magnitude shorter than Equation 21 (e.g. Wu & Murray 2003). For HD 209458b, the heating rate can be estimated to be far smaller than Jupiter's luminosity ( $3 \times 10^{24}$  erg) for gravitational tide synchronization timescales shorter than 1 Myr. Hence the magnetic spin-down torque and associated asynchronous rotation are not likely to give rise to a heating rate large enough to effect the thermal history of the planet significantly.

#### 4. TRANSIT DEPTHS IN LY $\alpha$

Section 3 described numerical solutions for the MHD variables  $\rho$  and  $\mathbf{v}$  for different model parameters. In this section the mass density  $\rho$  is converted into atomic hy-



drogen number density  $n_H$ , and the transmission spectra for the models in Table 2 are discussed.

As a point of departure when considering transmission spectra of the MHD simulation results, the simple model of Lecavelier Des Etangs et al. (2008) is first summarized. They consider a plane parallel, isothermal atmosphere with base radius  $R_b$  and altitude  $z = r - R_b$ . The number density is then  $n(z) = n_0 \exp(-z/H)$ , where  $H = k_b T / (\mu m_p g)$  is the scale height,  $\mu$  is the mean molecular weight, and  $g = GM_p / r^2$ . The path length through the atmosphere is  $\ell \simeq \sqrt{2\pi R_b H}$ , giving an optical depth  $\tau_\nu(z) = n_0 \sigma_\nu \ell \exp(-z/H)$ , where  $\sigma_\nu$  is the Ly $\alpha$  (1s  $\rightarrow$  2p) cross section. Setting  $\tau_\nu(z_\nu) = 1$  gives the altitude

$$z_\nu \simeq H \ln \left( \frac{1}{n_0 \sigma_\nu \sqrt{2\pi R_b H}} \right) \quad (22)$$

up to which the atmosphere is optically thick. The transit depth is then

$$\frac{R_p^2(\nu)}{R_\star^2} \simeq \frac{R_b^2 + 2R_b z_\nu}{R_\star^2}. \quad (23)$$

The altitude  $z_\nu \propto H \propto T/\mu g$ , so hot atmospheres of low mean molecular weight gas around planets with low gravity will have large scale heights and transit depths. Due to the steeply falling density, the transit depth has only a weak logarithmic dependence on  $\sigma_\nu$ .

For the Ly $\alpha$  transit depths of the MHD models considered here, the DZ is hydrostatic, but the tidal/rotational forces are important, and so gravity is weaker than  $GM_p/r^2$ . The corresponding larger scale heights make the plane parallel limit inaccurate, and the density profile, even of isothermal models, tends not to fall as steeply as it does deeper in the atmosphere. One consequence of the large scale heights is that there can be a significant contribution from gas with optical depth  $\tau \leq 1$ , but which occupies a large area. Hence, the ‘‘opaque disk’’ concept – that all absorption can be idealized as occurring inside the  $\tau = 1$  contour – may no longer be accurate. Hence, for careful work numerical integrations are required. However, the analytic model gives useful intuition and is simple.

#### 4.1. Details of the Calculation

Stellar Ly $\alpha$  photons passing through the planet’s atmosphere can be absorbed or scattered out of the line of sight to the observer, causing a decrease in flux. In addition, the interstellar medium (ISM) can absorb/scatter the light, most prominently in the Doppler core of the line. The spectrum observed at Earth is the combination of these two effects. If the in-transit flux is  $F_\nu$  and the out-of-transit flux is  $F_\nu^{(0)}$ , the fractional decrease in flux, the transit depth, is  $(F_\nu^{(0)} - F_\nu) / F_\nu^{(0)}$ .

The optical depth through the planet’s atmosphere is given by

$$\tau_\nu(y, z) = \int dx n_H(x, y, z) \sigma_\nu(x, y, z) \quad (24)$$

where  $n_H$  is the number density of the atomic hydrogen in the 1s state,  $x$  specifies the direction along the line of sight to the star,  $y$  and  $z$  are the perpendicular coordinates on the sky. This line profile is taken to be a Voigt

function (e.g. Rybicki & Lightman 1979) evaluated using the isothermal temperature  $T$ , and bulk fluid velocity is included by transforming the photon frequency from the planet frame to the rest frame of the fluid.

The transit depth will be expressed in terms of a frequency dependent planet radius,  $R_p(\nu)$ , which is defined as the radius of an opaque disk that is required to produce the same transit depth as the integral over the model atmosphere:

$$\frac{F_\nu^{(0)} - F_\nu}{F_\nu^{(0)}} \equiv \frac{R_p^2(\nu)}{R_\star^2} = \int_{\text{star}} dy dz \left[ 1 - e^{-\tau_\nu(y, z)} \right] \quad (25)$$

where corrections due to limb darkening have been ignored for simplicity. The fractional decrease in flux in Equation 25 is independent of ISM absorption, and depends solely on the planetary atmosphere. The integration over  $y$  and  $z$  extends over the stellar disk, where star has radius  $R_\star$ .

The frequency-integrated transit depth for the models is calculated as

$$\frac{\delta F}{F} = \frac{\int d\nu I_\nu^{(*)} \left( \frac{R_p(\nu)}{R_\star} \right)^2 e^{-\tau_\nu^{(\text{ISM})}}}{\int d\nu I_\nu^{(*)} e^{-\tau_\nu^{(\text{ISM})}}} \quad (26)$$

where

$$I_\nu^{(*)} = \left[ 1 + \left| \frac{\Delta v}{67 \text{ km s}^{-1}} \right|^3 \right]^{-1}. \quad (27)$$

is a fit to the shape of the Ly $\alpha$  intensity of the Sun under quiet solar conditions (Feldman et al. 1997). In units of velocity from line center at frequency  $\nu_0$ ,  $\Delta v = c(\nu - \nu_0)/\nu_0$ . The limits of integration in Equation 26 are  $-200 \text{ km s}^{-1} \leq \Delta v \leq 200 \text{ km s}^{-1}$  as in Ben-Jaffel (2008). The ISM optical depth  $\tau_\nu^{(\text{ISM})}$  is computed using the Voigt line profile evaluated with a temperature  $T_{\text{ism}} = 8000 \text{ K}$  and a neutral hydrogen column  $N_{\text{H,ism}} = 10^{18.4} \text{ cm}^{-2}$  (Wood et al. 2005). The Ly $\alpha$  line is completely absorbed within  $\Delta v \simeq \pm 50 \text{ km s}^{-1}$  from line center by the ISM.

The HI number density  $n_H(x, y, z)$  is computed by assuming a balance between optically-thin photoionization and radiative recombination (cf. Paper I, Section 8),

$$J_0 n_H = \alpha_B n_e n_p, \quad (28)$$

where  $J_0 \approx (6 \text{ hr})^{-1} (0.047 \text{ AU}/D)^2$  is the ionization rate for a Solar EUV spectrum (Paper I), and  $\alpha_B(T) \simeq 2.6 \times 10^{-13} \text{ cm}^3 \text{ s}^{-1} (10^4 \text{ K}/T)^{0.8}$  is the case B radiative recombination rate (Osterbrock & Ferland 2006). Assuming charge neutrality,  $n_e = n_p$ , and setting  $\rho = m_p(n_p + n_H)$ , Equation 28 has the analytic solution

$$n_H = \left[ \frac{\sqrt{J_0/\alpha_B + 4\rho/m_p} - \sqrt{J_0/\alpha_B}}{2} \right]^2 \quad (29)$$

At a number density  $n_{\text{eq}} = J_0/\alpha_B$  the gas at density  $\rho$  is 50% ionized with  $n_H = n_p$ . For  $n_H \gtrsim n_{\text{eq}}$ , the gas is mostly neutral, and vice versa for  $n_H \lesssim n_{\text{eq}}$ . The use of a constant  $J_0$  above simplifies the problem by requiring only the local gas density  $\rho$  to evaluate  $n_H$ .

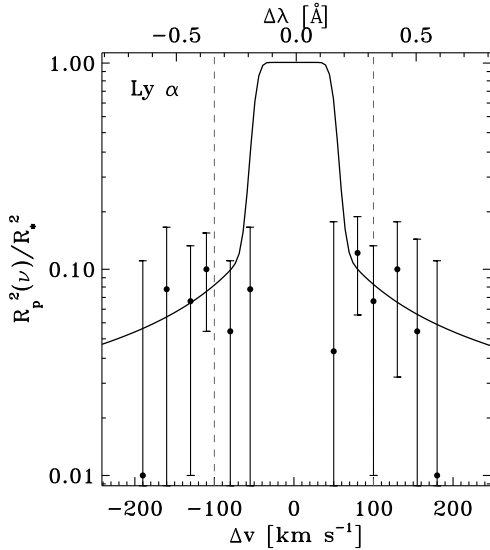


FIG. 6.— Model 1 transit curve for comparison to the transit depths for HD 209458b from Ben-Jaffel (2008).

#### 4.2. Results for HD 209458b

Figure 6 compares the Ly $\alpha$  transit radius versus wavelength for the fiducial Model 1 to HST STIS data from Ben-Jaffel (2008). Points near line center are heavily contaminated by ISM absorption and geocoronal emission and are omitted. Model 1 was designed to agree with the data through adjusting  $P_{ss}$  and  $a$  (see Table 3). The integrated transit depth,  $\delta F/F \approx 10\%$  (see Table 3), is in good agreement with Ben-Jaffel (2008) and Vidal-Madjar et al. (2008).

Figure 7 shows  $R_p(\nu)$  versus wavelength for some of the models from Table 2. The left (right) panel shows the effect of changing  $B_0$  ( $D$ ), holding all other parameters fixed. The model number for each line is given in the figure caption. For clarity, Doppler shifts  $\Delta\nu = v_x(\nu - \nu_0)/c$  due to line of sight motion were ignored in  $\sigma_\nu$  in the left panel, but are included in the right panel, to assess the role of the tidal force in accelerating the fluid. Bulk fluid motion is able to increase the cross section significantly at wavelengths on the steeply falling part of the Doppler core, roughly within  $\Delta\nu = \pm 50$  km/s of line center.

First consider the effect of the magnetic field in the left panel of Figure 7. There is little difference between the  $B_0 = 1$  and 10 G models, but in the range  $B_0 = 10 - 100$  G, the transit depth is observed to grow on the wings of the line. Since bulk fluid velocity effects have been omitted, the increase in transit depth must be due to an increase in hydrogen column over a large area surrounding the planet. Relative to  $B_0 = 10$  G, there is an increase in  $\delta F/F$  of 50% for the  $B_0 = 50$  G model and 250% for the  $B_0 = 100$  G model. This result clearly shows that the planetary magnetic field can have an important effect on the transit depth.

In the present paper, the base pressure and isothermal temperature are parameters of the model, and the transit depth is most sensitive to these two parameters. The range of these parameters (Table 2) was based on the detailed one-dimensional hydrostatic models, including ionization and heating/cooling balance, presented in Paper 1. More complete MHD simulations including heat-

ing and cooling would determine these quantities self-consistently as part of the solution, and for a given stellar EUV heating rate they would no longer be parameters. In such more complete models, the magnetic field would still be an essentially unconstrained parameter, as it is not measured or constrained by any observation as yet. Figure 7 shows that, if  $B_0$  was the main uncertainty in the model, an upper limit may be placed on magnetic field so that the transit depth is not too large compared to observations. For the fiducial parameters adopted for HD 209458b, that upper limit would be  $B_0 \approx 50$  G. However, we caution the reader that the large uncertainty in thermal structure due to uncertainty in stellar EUV and accelerated particles fluxes likely limit the practical ability to constrain the planetary magnetic field. Nevertheless, for the parameters used in this paper, sufficiently strong magnetic fields may in principle have a strong effect on the transit depth.

Next consider the effect of changing the rotation rate and tidal force, by changing  $D$  with all other parameters held fixed. Comparison of the Model 1 lines (solid black line) in the left and right panels shows that Doppler shifts due to bulk velocity in the WZ are small for the fiducial model and the model in which the planet has been moved outward. However, moving the planet inward by 25% to  $D = 0.035$  AU has the effect of broadening the wavelength range where  $R_p(\nu)$  is large (compare the dashed orange and solid black lines). This is due to bulk fluid velocities Doppler shifting those wavelengths to the Doppler core, where the cross section is large.

Gas that has escaped from the planet may still be strongly bound to the star, and may achieve high bulk velocity due to the gravity of the star. In the present case where the tidal force has been axisymmetrized, the effect is symmetric on either side of the line. In the 3D case, red-shifted absorption due to gas falling toward the star may achieve even larger velocities. For the chosen box-sizes  $r \sim 30R_p$ , the tidal force can accelerate fluid to poloidal velocities  $\simeq \Omega_p r \simeq 60$  km s $^{-1}$  in the simulation box. For larger box sizes, even higher velocities may be achieved. However, it is unclear from the present simulations if bulk velocities  $\gtrsim 100$  km s $^{-1}$  in the flow can affect the line profile, since the steeply falling gas density may not be sufficiently large to give  $\tau_\nu \gtrsim 1$  at such large distances from the planet. A further uncertainty is the interaction with the stellar wind, which may confine the planetary wind to smaller radii, with smaller acceleration by the tidal force.

To understand the role of magnetic fields on the transit depths, contours of optical depth  $\tau_\nu(y, z)$  at 100 km/s from line center are shown in the  $y$ - $z$  plane in Figures 8 and 9. The contours are evenly spaced in  $\log \tau$ , and white dashed lines show the  $\tau = 0.1, 1$  contours. The area enclosed by the  $\tau \gtrsim 1$  contour is optically thick, and contributes significantly to the transit depth. The region between  $\tau = 0.1 - 1$  contributes to the transit depth proportional to  $\text{area} \times \tau_\nu$ , and so may contribute significantly if the increase in area can overcome the decrease in optical depth. For this to occur, the density must not decrease too rapidly outward from the planet. Nearly the entire planetary upper atmosphere is optically thick when observed near line center ( $\Delta\nu = 0$ ), but moving away from line center the transit depth falls rapidly

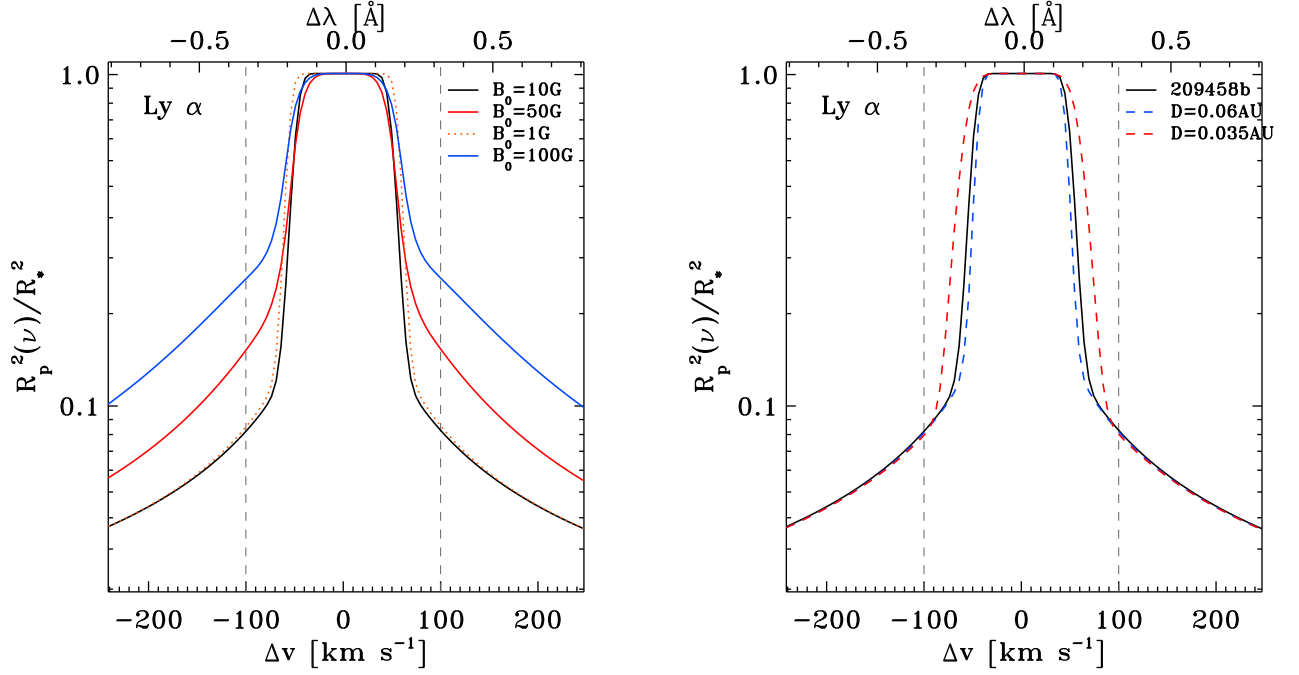


FIG. 7.— Ly $\alpha$  transit depth (Equation 25) versus wavelength in velocity units for selected models. The left panel compares models with different  $B_0$  (Model 1,  $B_0 = 10$  G, solid black line; Model 2,  $B_0 = 1$  G, dotted orange line; Model 3,  $B_0 = 50$  G, solid red line; Model 10,  $B_0 = 100$  G, solid blue line), while the right panel compares models with different  $D$  (Model 1,  $D = 0.047$  AU, solid black line; Model 8,  $D = 0.035$  AU, dashed red line; Model 9,  $D = 0.06$  AU, dashed blue line). In each panel, only the one parameter is changed, with all others held fixed at Model 1 values. For clarity, bulk Doppler shifts are ignored in the left panel; they only affect the line profile at  $\Delta v \lesssim 50$  km s $^{-1}$  from line center. Bulk Doppler shifts are included in the right panel, as the tidal force may give rise to additional acceleration. Vertical lines are placed at  $\Delta v = \pm 100$  km s $^{-1}$  for reference.

once the atmosphere becomes optically thin, which occurs at a different value of  $\Delta v$  for the range of models shown.

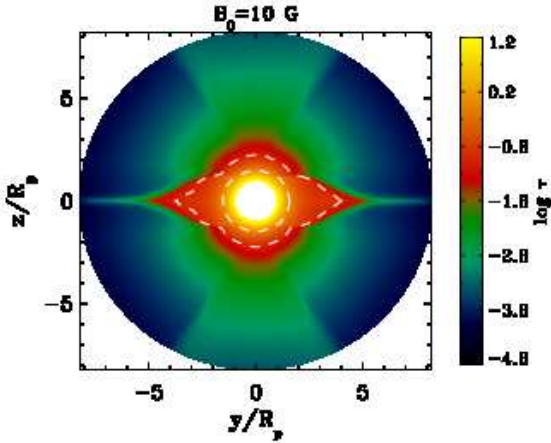


FIG. 8.— Contours of Ly $\alpha$  optical depth  $\tau(y, z)$  at  $\Delta v = 100$  km/s from line center for the steady-state simulation results from Model 1. The inner (outer) dashed white line shows  $\tau = 1$  (0.1).

Figure 8 shows the steady-state result for Model 1 ( $B_0 = 10$  G) at an illustrative frequency corresponding to 100 km/s from the line center. A large equatorial DZ with  $\tau \sim 0.1 - 1$  extends out to  $r = 4R_p$ , while the same contour only extends to  $r = 2R_p$  at the poles. The gas in the mid-latitude WZ has significantly smaller optical depth compared to points in the neighboring po-

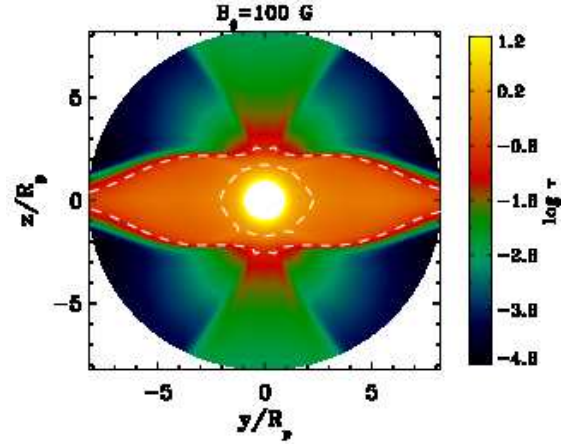


FIG. 9.— Same as Figure 8 for the Model 10.

lar and equatorial DZ's. The left-right asymmetry, most apparent in the  $\tau = 0.1$  contour, is due to the gas rotation Doppler shift in the cross section. Photons passing through the right side are shifted closer to line center, increasing the cross section, causing the contours to move further from the planet, and vice versa for the left side.

Figure 9 shows the steady-state results for the stronger field Model 10 ( $B_0 = 100$  G). The  $\tau = 0.1$  contour surrounding the equatorial DZ now extends to a significantly larger area which is sufficient to overcome the smaller optical depth there. Again, the mid-latitude WZ and polar DZ have far smaller optical depth compared to the equatorial DZ. A comparison of Figures 8 and 9 clearly shows the growth of the optically thick equatorial DZ, which

explains the increase in transit depth above  $B_0 \simeq 10$  G seen in the left panel of Figure 7.

Figures 8 and 9 clearly show the contribution to the transit depth from the DZ and WZ at a single, illustrative photon frequency ( $100 \text{ km s}^{-1}$  from line center). It is of interest to know what contribution the DZ and WZ make at all other wavelengths, and which wavelengths contribute most to the integrated transit depth in Equation 26. A technical point is that in order to know if a certain point is inside the DZ (WZ), one must trace along the field line to determine if it is closed (open), and if the fluid velocity is everywhere small (or accelerates to the sonic point). A simpler but approximate approach, followed here, is to compare the transit depth due to “slow” and “fast” material. The dividing line between the two is set by a threshold  $v_{p,\text{thr}}$  on the poloidal velocity; slow material has  $v_p \leq v_{p,\text{thr}}$  and vice versa for fast material. The slow material does not strictly trace out the DZ, since the fluid velocity at the base of the WZ is also small. By examination of optical depth contour plots using different velocity thresholds, we find that  $v_{p,\text{thr}} = 0.1a$  leads to only a small amount of slow material at the base of the WZ. Given the optical depths  $\tau_{\text{slow,fast}}(y, z)$  for the slow and fast material, the integrand of Equation 26 can be computed. Note that while the optical depth is linear in the contribution from slow and fast material, the transit depth  $\delta F/F$  is not, since  $\tau$  occurs in an exponent.

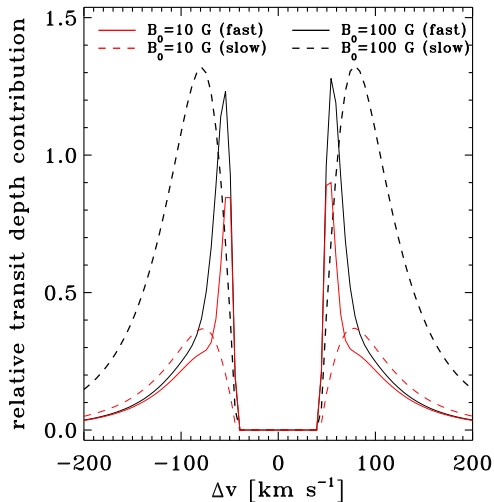


FIG. 10.— Integrand of the transit depth  $\delta F/F$  in Equation 26, broken into the contribution from “slow” fluid with  $v_p \leq 0.1a$  and “fast” fluid with  $v_p > 0.1a$ . Two magnetic field strengths are shown: Model 1 ( $B_0 = 10$  G) and Model 10 ( $B_0 = 100$  G).

Figure 10 shows the integrand of Equation 26, separated into slow and fast material, and computed for two different field strengths, Model 1 (10 G) and Model 10 (100 G). First consider the  $B_0 = 10$  G lines. The contribution from the slow material shows the expected peak near  $100 \text{ km s}^{-1}$ , with small contribution at large  $\Delta v$  due to small stellar flux, as well as near line center, due to ISM absorption. The fast material shows narrow peaks just outside the region of ISM absorption. This is due to poloidal fluid motions Doppler shifting the pho-

tons from the Lorentzian wing back into the Doppler core of the line, where the cross-section increases rapidly toward line center. Even though the slow and fast materials make comparable contribution to the frequency-integrated transit depth (i.e., the areas under the dashed and solid curves are comparable), the shapes of the relative transit depth profiles are very different. This difference can in principle provide a way to distinguish the absorption due to slowly moving DZ material and fast moving WZ material. Next, comparing the  $B_0 = 10$  and  $100$  G lines shows the far larger transit depth for the strong field case. This is due to the increased density at large radii, which is the result of the larger dead zone extending out to a region where the gravity  $-\nabla U_{\text{rot}}$  becomes quite small, so that the scale height is large and the density nearly constant. For the fast material, the higher field case shows absorption further from line center due to the higher poloidal velocity as the field is increased (see Figure 2).

Having investigated the transit spectra in detail, the mass and angular momentum loss rates are now considered. Comparing the values of  $\dot{M}$  and  $\dot{J}$  to  $\delta F/F$  in Table 3, the dominant effect is that higher  $P_{\text{ss}}$  and  $a$  lead to both larger  $\dot{M}$  and  $\dot{J}$ , as well as  $\delta F/F$ . This is due to the higher gas density. The role of magnetic field well into the strongly magnetized regime is also clear, in that larger  $B_0$  leads to larger  $\delta F/F$  and  $\dot{J}$ , and slightly smaller  $\dot{M}$ .

How well did the semi-analytic solutions for  $\rho$  and  $\mathbf{v}$  in Paper I do at predicting the shape of the magnetospheres and the optical depth contours? Recall that in Paper I an inner dipole field was fitted to an outer monopole to represent the transition between wind and dead zones. The size of the dead zone was found by stress balance at the equatorial cusp point. Figure 14 of Paper I shows the hydrogen column for a set of models, and can be compared to the optical depth contours in Figures 8 and 9. Model 1 (6) of Paper I is similar to Model 1 (3) here. The 3-zone structure is evident on both treatments, and many of the trends, e.g. the growth of the equatorial DZ, are evident in both. One key difference is that the equatorial DZ looks more “cuspy” in the simulations where the field is self-consistently calculated, while the semi-analytic calculations give round-shaped dead zones. The dead zone sizes in the two calculations are comparable. The shapes of the wind zones differ between the two calculations due to the different shapes of the field lines, since the poloidal velocity is parallel to the poloidal field. Overall, the semi-analytic methods of paper I give results in rough quantitative agreement with the simulations here, at least near the planet where the assumed field shape of Paper I is approximately correct. Further from the planet, the backward bending of field lines, and the deviations from corotation become large, and are not taken into account in Paper I.

#### 4.3. Results for HD 189733b

Lecavelier Des Etangs et al. (2010) used the HST ACS to measure an integrated transit depth of 5% in the Ly $\alpha$  line, smaller than the transit depth of HD 209458b by a factor  $\simeq 2$ . In this section the exercise from Section 4.2 is repeated for the planet HD 189733b, and the effect of different  $M_p$ ,  $R_p$  and  $D$  is discussed. The plan-

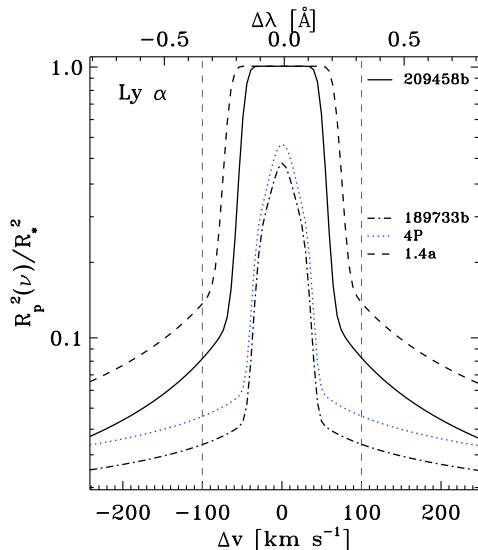


FIG. 11.— The fiducial model for HD 209458b in comparison to three models for HD 189733b. The dot-dashed line is the frequency-dependent transit depth for parameters matched to HD 189733b, while the blue-dotted and dashed lines vary the base density and sound speed, respectively.

etary mass and radius are set to  $M_p = 1.14 M_J$  and  $R_p = 1.14 R_J$ , and the semi-major axis is  $D = 0.031$  AU (<http://exoplanet.eu/catalog>). The Jean’s parameter  $\lambda = GM_p/R_p a^2$  is a factor  $\simeq 2$  larger for HD 189733b than HD 209458b, for the same  $a$ .

Figure 11 compares the transit depth for the fiducial Model 1 of HD 209458b to three models for HD 189733b: a fiducial model with  $P_{ss}$ ,  $a$  and  $B_0$  identical to that of Model 1 of HD 209458b; a model with pressure 4 times larger; and a model with sound speed 40% larger. The larger base pressure and sound speed are motivated by the higher stellar EUV flux for HD 189733b (Sanz-Forcada et al. 2011), due to the closer orbital separation, as well as higher stellar activity.

The fiducial model for HD 189733b has smaller transit depth ( $\delta F/F = 0.04$ ) than that of Model 1 for HD 209458b ( $\delta F/F = 0.1$ ), due to the larger  $M_p/R_p$  for HD 189733b causing the density to decrease outward faster. The transit depth is surprisingly close to the observed value. Since the EUV flux is higher, both the base pressure and temperature are expected to be higher than the HD 209458b case. As an illustration, increasing the base pressure slightly has the effect of increasing the density everywhere, leading to larger transit depth ( $\delta F/F = 0.05$ ) comparable to the observed value for HD 189733b. Lastly, increasing the sound speed by 40% gives the model the same  $\lambda$  as Model 1 of HD 209458b. The higher transit depth ( $\delta F/F = 0.24$ ), as compared to Model 1 of HD 209458b, is due, at least in part, to a stronger stellar tide (see Table 3).

## 5. SUMMARY

The MHD wind model simulations presented in this paper demonstrate that, for an extended range of latitudes, the planet’s magnetic field can qualitatively change the properties of a thermally-driven outflow. In Paper I, dipole field geometry and expected field strengths of hot Jupiters were used to estimate the size of the closed field line regions, where an outflow is quenched by rigid mag-

netic field lines. The inclusion of the stellar tide was also shown to quench the outflow in the polar region due to the higher potential barrier. The estimated equatorial dead-zone sizes were  $\sim 3 - 10 R_p$  for the parameters of interest.

MHD simulations permitted the relaxation of a prescribed field geometry, as hydrodynamic stresses and magnetic stresses in the thermally-driven outflow from the hot inner boundary were computed self-consistently through force balance both across and along field lines. The simulation results verify the main features of the semi-analytic models of Paper I, including the dependence of their structure of the upper atmosphere on  $B_0$  (Figures 1 and 2) and stellar tide strength (Figures 3 and 4). The MHD wind model also permitted a self-consistent calculation of the mass and angular momentum loss rates, which were presented in Section 3.3 for different stellar tide strengths and field strengths, and the integrated Ly $\alpha$  transit depth,  $\delta F/F$  (the observable quantity, see Section 4). The results are most consistent with a pressure of 50-60 nbar and a temperature of  $\sim 10^4$  K at the base of the thermosphere for HD 209458b, corresponding to a mass loss rate  $\dot{M} \simeq 3 \times 10^{11}$  g s $^{-1}$  and an angular momentum loss rate  $\dot{J} \simeq 6 \times 10^{28}$  g cm $^2$  s $^{-2}$ .

A central result of this paper is that for sufficiently large magnetic field, the large resulting equatorial DZ may dominate the optically thick area which gives rise to the transit depth signal. In this strongly magnetized regime, we find that the transit depth increases with the magnetic field. If the thermal structure were well known, this strong dependence on the magnetic field would allow an upper limit to be placed on the planet’s magnetic field so as not to over-predict the transit depth. However, due to uncertainties in heating rates due to stellar EUV and accelerated particles, such an exercise is likely not possible. However, the parameter study in this paper does make it clear what magnetic field strength is required to increase the transit depth in the parametrized models, which may be compared to the thermal structure in more realistic models.

A consequence of the existence of a large DZ in the strong field case is that Ly $\alpha$  absorption occurring out to near the Roche-lobe radius does *not* directly imply the absorbing gas is escaping (e.g. Vidal-Madjar et al. 2003), as emphasized in Paper I. The MHD model (both analytic and numerical) does exhibit gas in the mid-latitude WZ which is escaping, however, the Ly $\alpha$  transmission spectrum is less sensitive to the gas in this region as the optical depths are lower (see Figure 9).

Because of large observational uncertainties, the transit depth as a function of wavelength cannot precisely constrain the pressure at the base of the warm H layer (see Figure 7). The integrated transit depths computed from the model Ly $\alpha$  spectra presented in Section 4 provided another quantitative comparison with observations. The high sensitivity of the integrated transit depth on the pressure at the base of the warm H layer suggests that this observable quantity can probe and constrain the conditions in the thermosphere of highly irradiated hot Jupiters. At the same time, the numerical models presented here provide complementary information about the resulting expected mass and angular momentum loss rates, which are inaccessible by observations.

The authors thank Duncan Christie and David Sing for helpful conversations. The authors also thank the referee for a thoughtful and thorough report which improved this

paper. This work was supported in part by NSF (AST-0908079) and NASA Origins (NNX10AH29G) grants.

#### APPENDIX

##### SHEAR LAYER AND CURRENT SHEET NEAR THE EQUATORIAL DEAD-ZONE/WIND-ZONE BOUNDARY

At the boundary between the equatorial DZ and mid-latitude WZ, there are sudden changes in fluid velocity and magnetic field over short distance. The origin of this shear layer and current sheet was discussed in Section 3.1. As the simulations presented in this paper do not include explicit viscous forces and Ohmic diffusion, it is the grid-scale numerical effects contained with the ZEUS-MP code that control the behavior of the solutions at these discontinuities.

The possible effects from numerical diffusion came to our attention due to the spurious bump in density at the equator shown in Figure 5, where a rise in density occurs inside the Hill radius. This behavior contradicts basic analytic considerations. It was shown in the Appendix of Paper I that, in steady state, the Bernoulli constant

$$W \equiv \frac{1}{2}v^2 + a^2 \ln \rho + U_{\text{rot}} \quad (\text{A1})$$

(where  $v$  and  $U_{\text{rot}}$  are defined in a frame corotating with the planet) must be a constant along a given field line in the dead-zone (see Equation A10 of Paper I). Since  $v = 0$ , our choice of base density, Equation 9, indicates that  $W$  should be a constant throughout the dead-zone. The force-balance equation A8 of Paper I implies immediately that the Lorentz force must vanish in the dead-zone. If this is the case, the density along the equator can only increase with distance outside the Hill radius. This contradicts the numerical results in Figure 5.

The spurious density bump seems to be due to numerical effects near the dead-zone/wind-zone boundary, although the origin is rather subtle. In hindsight, it is not surprising that the boundary would be difficult to treat numerically, because there are discontinuities in all quantities: density and each of the three components of the velocity and magnetic field. The discontinuity in magnetic field, in particular, is difficult to treat accurately (see, e.g., Fig. 16 of Stone & Norman 1992b). One way to increase the accuracy is to increase the spatial resolution, which we have done for the fiducial Model 1. In Fig. 12, we show the equatorial density profile at four different resolutions ( $100 \times 100$ ,  $272 \times 200$ ,  $400 \times 400$ , and  $800 \times 800$ ), normalized by the substellar point density. It is clear that the spurious density enhancement decreases with increasing resolution, although even at  $800 \times 800$  it does not disappear completely.

This density enhancement is caused by magnetic forces (see Fig. 13), which should vanish throughout the dead-zone according to the analytic considerations mentioned earlier. At the heart of these considerations is the constancy of the Bernoulli constant  $W$  throughout the dead-zone. It breaks down in the numerical simulations, as illustrated in Figure 14, where we show the distribution of the Bernoulli constant and poloidal velocity for a selected region for the standard resolution  $272 \times 200$ . Note that  $W$  is indeed very close to the expected value over most of the dead-zone (where the poloidal velocity is small, see the right panel), except in a layer near the DZ/WZ boundary, where deviation of order 1% is evident; this is also the region where the magnetic forces become appreciable, and the density starts to increase outward spuriously. As the resolution increases, the boundary layer shrinks in size. This should serve as a cautionary tale for future simulations of hot Jupiter magnetospheres, especially in 3D, where the resolution will necessarily be coarser than in 2D. Nevertheless, the basic three-zone structure of the magnetosphere is robust.

Although the density profile in the equatorial DZ is resolution dependent, the transit depth for the four models shown in Figure 12 varies only slightly, with values  $\delta F/F = 0.0943, 0.1002, 0.1026, 0.1031$  for resolutions  $100 \times 100$ ,  $272 \times 200$  (Model 1),  $400 \times 400$  and  $800 \times 800$ . This variation with resolution is far less than the variation from changing parameters in Models 1-9. It lends confidence that the broad conclusions are not affected much by finite numerical resolution effects.

#### REFERENCES

- Ballester, G. E., Sing, D. K., & Herbert, F. 2007, *Nature*, 445, 511  
 Ben-Jaffel, L. 2007, *ApJ*, 671, L61  
 Ben-Jaffel, L. 2008, *ApJ*, 688, 1352  
 Ben-Jaffel, L., & Sona Hosseini, S. 2010, *ApJ*, 709, 1284  
 Blandford, R. D., & Payne, D. G. 1982, *MNRAS*, 199, 883  
 Braginskii, S. I. 1965, *Reviews of Plasma Physics*, 1, 205  
 Charbonneau, D., Brown, T. M., Noyes, R. W., & Gilliland, R. L. 2002, *ApJ*, 568, 377  
 Christensen, U. R., Holzwarth, V., & Reiners, A. 2009, *Nature*, 457, 167  
 Dalgarno, A., & McCray, R. A. 1972, *ARA&A*, 10, 375  
 Ehrenreich, D., & Désert, J.-M. 2011, *A&A*, 529, A136  
 Ehrenreich, D., Lecavelier Des Etangs, A., Hébrard, G., Désert, J.-M., Vidal-Madjar, A., McConnell, J. C., Parkinson, C. D., Ballester, G. E., & Ferlet, R. 2008, *A&A*, 483, 933  
 Ekenbäck, A., Holmström, M., Wurz, P., et al. 2010, *ApJ*, 709, 670  
 Feldman, U., Behring, W. E., Curdt, W., Schuehle, U., Wilhelm, K., Lemaire, P., & Moran, T. M. 1997, *ApJS*, 113, 195  
 Fossati, L., et al. 2010, *ApJ*, 714, L222  
 France, K., Linsky, J. L., Yang, H., Stocke, J. T., & Froning, C. S. 2011, *Ap&SS*, 335, 25  
 García Muñoz, A. 2007, *Planet. Space Sci.*, 55, 1426  
 Gold, T. 1959, *J. Geophys. Res.*, 64, 1219  
 Grießmeier, J.-M., Stadelmann, A., Penz, T., et al. 2004, *A&A*, 425, 753  
 Gu, P.-G., Lin, D. N. C., & Bodenheimer, P. H. 2003, *ApJ*, 588, 509  
 Hapke, B. 1993, *Topics in Remote Sensing*, Cambridge, UK: Cambridge University Press, —c1993,  
 Hayes, J. C., Norman, M. L., Fiedler, R. A., Bordner, J. O., Li, P. S., Clark, S. E., ud-Doula, A., & Mac Low, M.-M. 2006, *ApJS*, 165, 188  
 Heinemann, M., & Olbert, S. 1978, *J. Geophys. Res.*, 83, 2457  
 Henry, G. W., Marcy, G. W., Butler, R. P., & Vogt, S. S. 2000, *ApJ*, 529, L41  
 Heyvaerts, J., & Norman, C. 1989, *ApJ*, 347, 1055  
 Holmström, M., Ekenbäck, A., Selsis, F., et al. 2008, *Nature*, 451, 970  
 Ip, W.-H., Kopp, A., & Hu, J.-H. 2004, *ApJ*, 602, L53

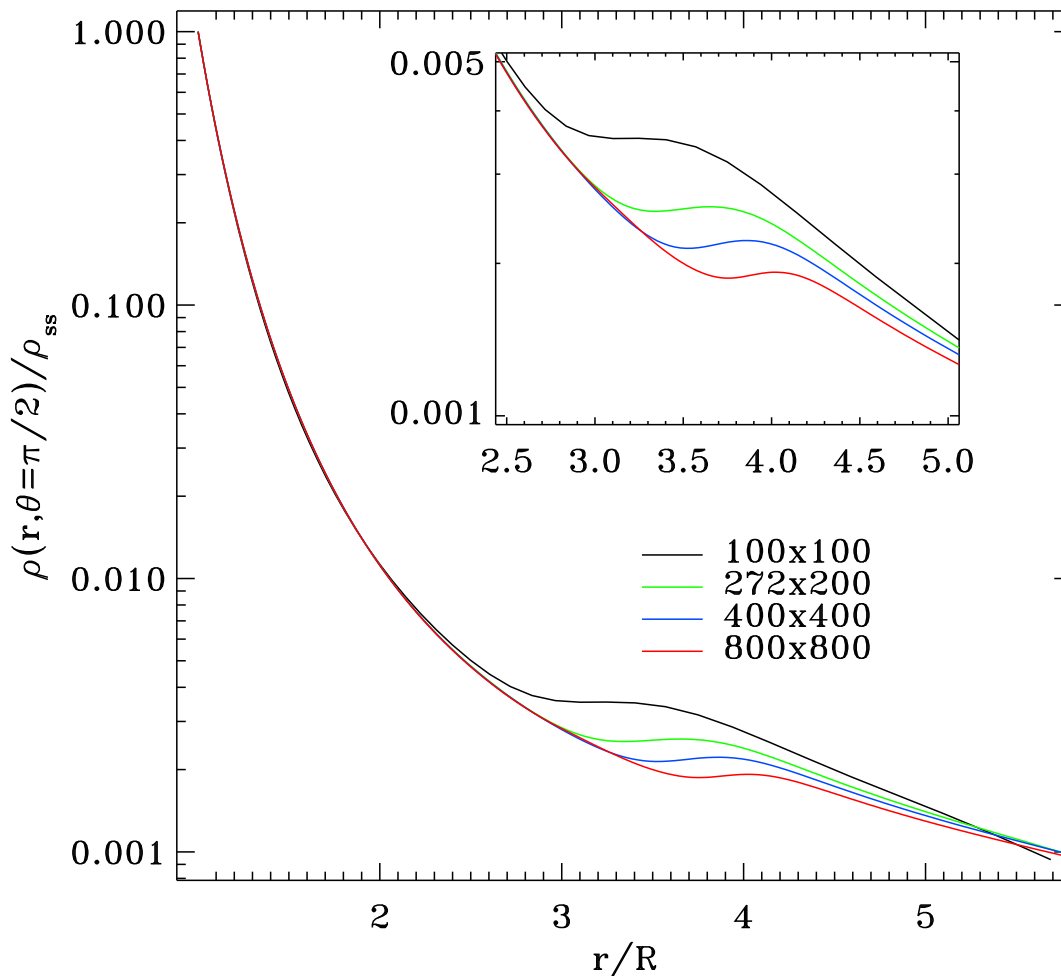


FIG. 12.— The equatorial density profile for Model 1 at three different grid resolutions in steady-state, as well as an inset that shows a more detailed view of a region from  $2.5 < r/R_p < 5$ .

- Jensen, A. G., Redfield, S., Endl, M., et al. 2011, *ApJ*, 743, 203  
 Jensen, A. G., Redfield, S., Endl, M., et al. 2012, *ApJ*, 751, 86  
 Kivelson, M. G., & Russell, C. T. 1995, *Introduction to Space Physics*, Edited by Margaret G. Kivelson and Christopher T. Russell, pp. 586. ISBN 0521451043. Cambridge, UK: Cambridge University Press, April 1995.,  
 Koskinen, T. T., Yelle, R. V., Lavvas, P., & Lewis, N. K. 2010, *ApJ*, 723, 116  
 Lai, D., Helling, C., & van den Heuvel, E. P. J. 2010, *ApJ*, 721, 923  
 Lamers, H. J. G. L. M., & Cassinelli, J. P. 1999, *Introduction to Stellar Winds*, by Henny J. G. L. M. Lamers and Joseph P. Cassinelli, pp. 452. ISBN 0521593980. Cambridge, UK: Cambridge University Press, June 1999.  
 Lecavelier Des Etangs, A., Pont, F., Vidal-Madjar, A., & Sing, D. 2008, *A&A*, 481, L83  
 Lecavelier des Etangs, A., Bourrier, V., Wheatley, P. J., et al. 2012, *A&A*, 543, L4  
 Lecavelier Des Etangs, A., et al. 2010, *A&A*, 514, A72  
 Li, S.-L., Miller, N., Lin, D. N. C., & Fortney, J. J. 2010, *Nature*, 463, 1054  
 Lin, D. N. C., Bodenheimer, P., & Richardson, D. C. 1996, *Nature*, 380, 606  
 Linsky, J. L., Yang, H., France, K., et al. 2010, *ApJ*, 717, 1291  
 Livio, M. 1997, *IAU Colloq. 163: Accretion Phenomena and Related Outflows*, 121, 845  
 Lovelace, R. V. E., Mehanian, C., Mobarry, C. M., & Sulkanen, M. E. 1986, *ApJS*, 62, 1  
 Lubow, S. H., & Shu, F. H. 1975, *ApJ*, 198, 383  
 Mercier, C., & Heyvaerts, J. 1977, *A&A*, 61, 685  
 Mestel, L. 1968, *MNRAS*, 138, 359  
 Mestel, L., & Spruit, H. C. 1987, *MNRAS*, 226, 57  
 Mihalas, D. 1978, *San Francisco*, W. H. Freeman and Co., 1978. 650 p.,  
 Murray-Clay, R. A., Chiang, E. I., & Murray, N. 2009, *ApJ*, 693, 23  
 Murray, C. D., & Dermott, S. F. 2000, *Solar System Dynamics*, by C.D. Murray and S.F. Dermott, Cambridge, UK: Cambridge University Press, 2000.,  
 Neubauer, F. M. 1998, *J. Geophys. Res.*, 103, 19843  
 Noyes, R. W., & Kalkofen, W. 1970, *Sol. Phys.*, 15, 120  
 Osterbrock, D. E., & Ferland, G. J. 2006, *Astrophysics of gaseous nebulae and active galactic nuclei*, 2nd. ed. by D.E. Osterbrock and G.J. Ferland. Sausalito, CA: University Science Books, 2006  
 Okamoto, I. 1974, *MNRAS*, 166, 683  
 Parks, G. K. 2004, *Physics of space plasmas : an introduction / George K Parks*. Boulder, Colo. : Westview Press, Advanced Book Program, c2004.,  
 Pneuman, G. W., & Kopp, R. A. 1971, *Sol. Phys.*, 18, 258  
 Preusse, S., Kopp, A., Büchner, J., & Motschmann, U. 2005, *A&A*, 434, 1191  
 Preusse, S., Kopp, A., Büchner, J., & Motschmann, U. 2007, *Planet. Space Sci.*, 55, 589  
 Pudritz, R. E., & Norman, C. A. 1983, *ApJ*, 274, 677  
 Ray, T. P. 2007, *IAU Symposium*, 243, 183

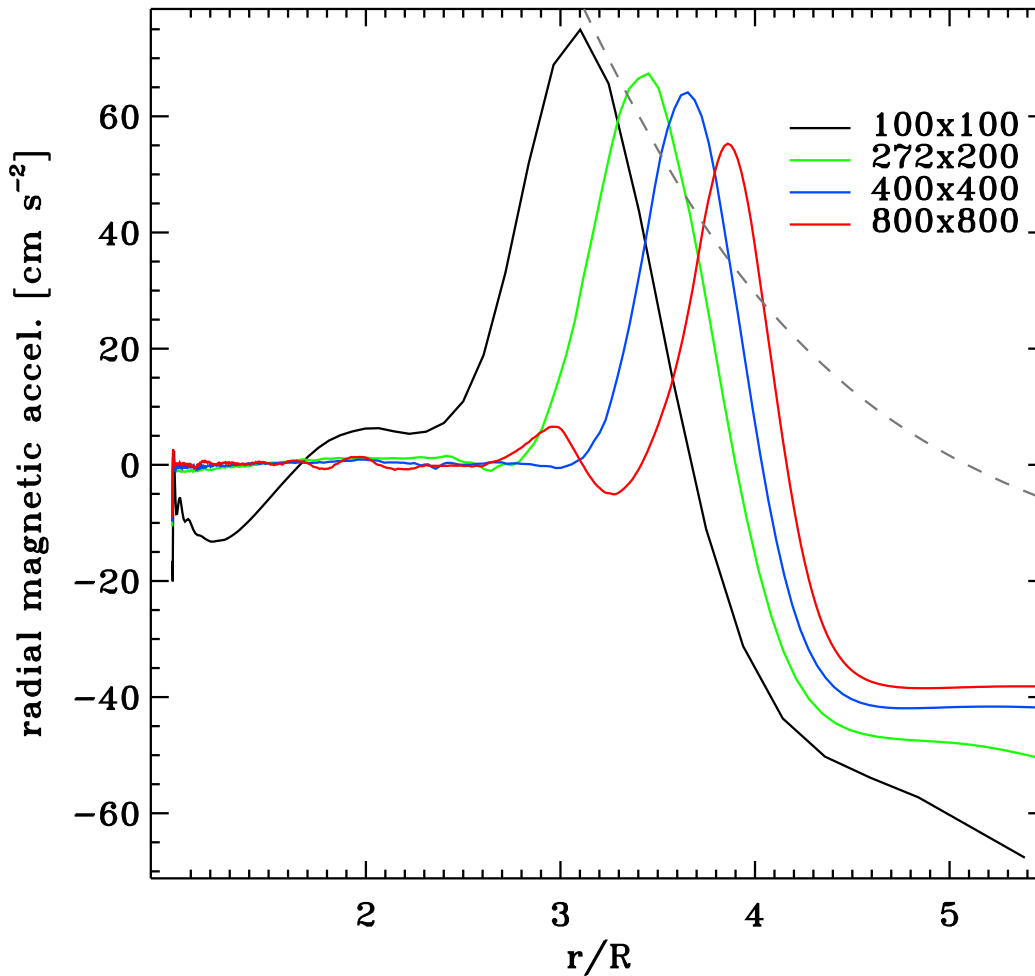


FIG. 13.— The radial magnetic forces along the equator for Model 1 at three different grid resolutions in steady-state. The gray dashed line represents the effective gravity.

Redfield, S., Endl, M., Cochran, W. D., & Koesterke, L. 2008, *ApJ*, 673, L87

Reiners, A., & Christensen, U. R. 2010, *A&A*, 522, A13

Rybicki, G. B., & Lightman, A. P. 1979, New York, Wiley-Interscience, 1979. 393 p.,

Sánchez-Lavega, A. 2004, *ApJ*, 609, L87

Saar, S. H., Cuntz, M., Kashyap, V. L., & Hall, J. C. 2008, *IAU Symposium*, 249, 79

Sanz-Forcada, J., Micela, G., Ribas, I., et al. 2011, *A&A*, 532, A6 (<http://sdc.cab.inta-csic.es/xexoplanets/jsp/homepage.jsp>)

Sing, D. K., Vidal-Madjar, A., Désert, J.-M., Lecavelier des Etangs, A., & Ballester, G. 2008, *ApJ*, 686, 658

Schunk, R. W. & Nagy, A. F. 2004, *Ionospheres (Ionosphere)*

Snellen, I. A. G., Albrecht, S., de Mooij, E. J. W., & Le Poole, R. S. 2008, *A&A*, 487, 357

Southworth, J. 2010, *MNRAS*, 408, 1689

Spruit, H. C. 1996, arXiv:astro-ph/9602022

Stone, J. M., Mihalas, D., & Norman, M. L. 1992, *ApJS*, 80, 819

Stone, J. M., & Norman, M. L. 1992a, *ApJS*, 80, 753

Stone, J. M., & Norman, M. L. 1992b, *ApJS*, 80, 791

Stone, J. M., & Proga, D. 2009, *ApJ*, 694, 205

Tian, F., Toon, O. B., Pavlov, A. A., & De Sterck, H. 2005, *ApJ*, 621, 1049

Trammell, G. B., Arras, P., & Li, Z.-Y. 2011, *ApJ*, 728, 152 (Paper I)

Tremblin, P., & Chiang, E. 2013, *MNRAS*, 428, 2565

Vidal-Madjar, A., Désert, J.-M., Lecavelier des Etangs, A., Hébrard, G., Ballester, G. E., Ehrenreich, D., Ferlet, R., McConnell, J. C., Mayor, M., & Parkinson, C. D. 2004, *ApJ*, 604, L69

Vidal-Madjar, A., Lecavelier des Etangs, A., Désert, J.-M., Ballester, G. E., Ferlet, R., Hébrard, G., & Mayor, M. 2003, *Nature*, 422, 143

—, 2008, *ApJ*, 676, L57

Winn, J. N., Suto, Y., Turner, E. L., Narita, N., Frye, B. L., Aoki, W., Sato, B., & Yamada, T. 2004, *PASP*, 56, 655

Woitak, J., Bacciotti, F., Ray, T. P., Marconi, A., Coffey, D., & Eisloffel, J. 2005, *A&A*, 432, 149

Wood, B. E., Redfield, S., Linsky, J. L., Müller, H.-R., & Zank, G. P. 2005, *ApJS*, 159, 118

Woods, T. N., Rottman, G. J., Bailey, S. M., Solomon, S. C., & Worden, J. R. 1998, *Sol. Phys.*, 177, 133

Wu, Y., & Murray, N. 2003, *ApJ*, 589, 605

Yan, M., Sadeghpour, H. R., & Dalgarno, A. 1998, *ApJ*, 496, 1044

Yelle, R. V. 2004, *Icarus*, 170, 167

Yelle, R. V. 2006, *Icarus*, 183, 508



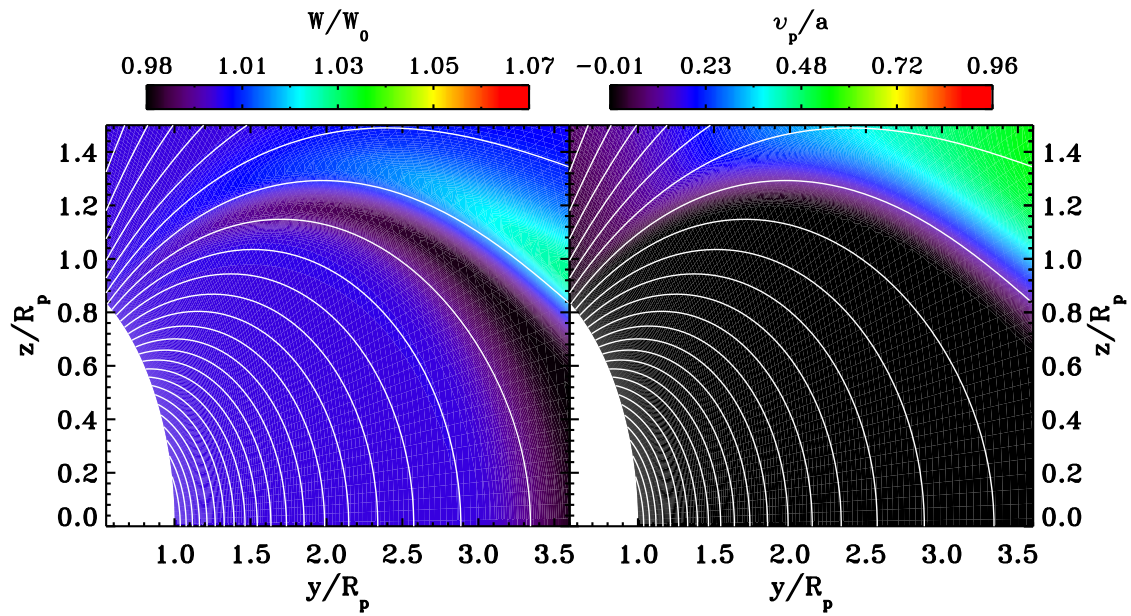


FIG. 14.— The variation of the Bernoulli constant relative to the base value for a region including the DZ/WZ boundary layer, and the poloidal velocity distribution for the same region.